CrossMark

Braving the Storm: Quantifying Disk-wide Ionized Outflows in the Large Magellanic Cloud with ULLYSES

Yong Zheng (郑永)[1] , Kirill Tchernyshyov[2] , Knut Olsen[3] , Yumi Choi[3] , Chad Bustard[4] , Julia Roman-Duval[5] ,
Robert Zhu[6] , Enrico M. Di Teodoro[7] , Jessica Werk[2] , Mary Putman[8] , Anna F. McLeod[9,10] , Yakov Faerman[2] ,
Raymond C. Simons[11] , and Joshua Peek[5]

[1] Department of Physics, Applied Physics and Astronomy, Rensselaer Polytechnic Institute, Troy, NY 12180, USA; zhengy14@rpi.edu
[2] Department of Astronomy, University of Washington, Seattle, WA 98195, USA
[3] National Optical Astronomy Observatory, Tucson, AZ 85719, USA
[4] Kavli Institute for Theoretical Physics, University of California—Santa Barbara, Kohn Hall, Santa Barbara, CA 93107, USA
[5] Space Telescope Science Institute, 3700 San Martin Drive, Baltimore, MD 21218, USA
[6] Department of Astronomy, University of California, Berkeley, CA 94720, USA
[7] Dipartimento di Fisica e Astronomia, Università degli Studi di Firenze, I-50019 Sesto Fiorentino, Italy
[8] Department of Astronomy, Columbia University, New York, NY 10027, USA
[9] Centre for Extragalactic Astronomy, Department of Physics, Durham University, South Road, Durham DH1 3LE, UK
[10] Institute for Computational Cosmology, Department of Physics, Durham University, South Road, Durham DH1 3LE, UK
[11] Department of Physics, University of Connecticut, 196A Auditorium Road Unit 3046, Storrs, CT 06269, USA
Received 2024 February 2; revised 2024 July 15; accepted 2024 July 15; published 2024 October 1

Abstract

The Large Magellanic Cloud (LMC) is home to many H II regions, which may lead to significant outflows. We examine the LMC's multiphase gas ($T\sim10^{4\text{-}5}$ K) in H I, S II, Si IV, and C IV using 110 stellar sight lines from the Hubble Space Telescope's Ultraviolet Legacy Library of Young Stars as Essential Standards program. We develop a continuum fitting algorithm based on the concept of Gaussian process regression and identify reliable LMC interstellar absorption over $v_{\rm helio} = 175\text{–}375$ km s^{-1}. Our analyses show disk-wide ionized outflows in Si IV and C IV across the LMC with bulk velocities of $|v_{\rm out,\ bulk}| \sim 20\text{–}60$ km s^{-1}, which indicates that most of the outflowing mass is gravitationally bound. The outflows' column densities correlate with the LMC's star formation rate surface densities ($\Sigma_{\rm SFR}$), and the outflows with higher $\Sigma_{\rm SFR}$ tend to be more ionized. Considering outflows from both sides of the LMC as traced by C IV, we conservatively estimate a total outflow rate of $\dot{M}_{\rm out} \gtrsim 0.03\ M_\odot\,{\rm yr}^{-1}$ and a mass-loading factor of $\eta \gtrsim 0.15$. We compare the LMC's outflows with those detected in starburst galaxies and simulation predictions, and find a universal scaling relation of $|v_{\rm out,\ bulk}| \propto \Sigma_{\rm SFR}^{0.23}$ over a wide range of star-forming conditions ($\Sigma_{\rm SFR} \sim 10^{-4.5}\text{–}10^2\ M_\odot\,{\rm yr}^{-1}\,{\rm kpc}^{-2}$). Lastly, we find that the outflows are corotating with the LMC's young stellar disk and the velocity field does not seem to be significantly impacted by external forces; we thus speculate on the existence of a bow shock leading the LMC, which may have shielded the outflows from ram pressure as the LMC orbits the Milky Way.

Unified Astronomy Thesaurus concepts: Large Magellanic Cloud (903); Stellar feedback (1602); Metal line absorbers (1032); Galaxy evolution (594); Interstellar medium (847)

Materials only available in the online version of record: *machine-readable table*

1. Introduction

Stellar feedback is a multiscale process. It requires a detailed understanding of small-scale star-forming regions, large-scale structures such as the interstellar medium (ISM), and the circumgalactic medium (CGM), as well as the delicate interplay among these gaseous structures (McKee & Ostriker 1977). Feedback-driven outflows enrich the CGM with metals, momentum, and energy; and, theoretical studies find that the presence of stellar feedback is key to producing a realistic galaxy and a gaseous CGM with multiphase properties consistent with observations (e.g., Vogelsberger et al. 2014; Hopkins et al. 2014; Schaye et al. 2015; Peeples et al. 2019).

Galactic outflows have been ubiquitously observed in star-forming galaxies (Veilleux et al. 2020). For example, the Na I 5890/5896 Å doublet probes dusty outflows with velocities up to ~1000 km s^{-1} in infrared (ultra)luminous starburst galaxies

(e.g., Heckman et al. 2000; Martin 2005; Rupke et al. 2005; Chen et al. 2010). These outflows tend to be neutral; otherwise, Na I would not exist with its ionization potential at 5.1 eV. Rubin et al. (2014) studied cool outflows ($T\sim10^4$ K) in star-forming galaxies at $0.3 < z < 1.4$ using Mg II and Fe II doublets and found an outflow detection rate of $\sim66\%$ (see also Weiner et al. 2009; Erb et al. 2012; Davis et al. 2023). Warmer ionized outflows ($T \sim 10^{4-5.5}$ K) in star-forming or starburst galaxies can be traced with numerous ions in the ultraviolet (UV) such as Si II, Si III, Si IV, C IV, and O VI with velocities up to a few hundreds of kilometers per second (e.g., Heckman et al. 2015; Chisholm et al. 2015; Xu et al. 2022; Sirressi et al. 2024). Though with different tracers, a common finding among the above studies is that the velocities of outflows, regardless of their phases, correlate significantly with host galaxies' star formation activities, stellar masses, and circular velocities.

For starburst galaxies, the bulk velocities of outflows correlate with the galaxies' star formation rates (SFRs) as a power law, $v_{\rm out,\ bulk} \propto {\rm SFR}^\alpha$, with $\alpha \sim 0.2\text{–}0.35$ (e.g., Martin 2005; Chisholm et al. 2015; Rupke 2018; Xu et al. 2022). The power-law index α is shallower when considering the correlation between $v_{\rm out,\ bulk}$ and SFR per surface area $\Sigma_{\rm SFR}$ ($\alpha \sim 0.1\text{–}0.2$)

Table 1
Key Physical Parameters of the LMC

Parameter	Value	Reference(s)
d (distance)	50.1 (kpc)	Freedman et al. (2001)
$v_{LMC, LSR}$ (systemic velocity)	264.0 ± 0.4 (km s^{-1})	Choi et al. (2022
$v_{LMC, G}$ (Galactocentric velocity)	321 ± 24 (km s^{-1})	Kallivayalil et al. (2013)
i (inclination)	23.4 ± 0.5 (deg)	Choi et al. (2022)
M_* (stellar mass)	3×10^9 ($M_\odot$)	van der Marel et al. (2002)
M_{HI} (H I gas mass)	4.4×10^8 ($M_\odot$)	Brüns et al. (2005)
Z (metallicity)	0.5 ($Z_\odot$)	Russell & Dopita (1992)
SFR (present day)	~ 0.2 ($M_\odot$ yr^{-1})	Harris & Zaritsky (2009)
$v_{rot,*}$ (stellar rotation[a])	77.5 ± 1.3 (km s^{-1})	Choi et al. (2022)
$v_{rot, H I}$ (H I rotation)	~ 70 (km s^{-1})	Kim et al. (1998)
R.A.[b] (J2000) (LMC center)	80.443 (deg)	Choi et al. (2022)
decl.[b] (J2000) (LMC center)	-69.272 (deg)	Choi et al. (2022)

Notes.
[a] The stellar rotation is fitted for a population of young red supergiants and evolved old red giant branch and asymptotic giant branch stars.
[b] The LMC's kinematic center is derived based on $\sim$10,000 red giant branch stars, asymptotic giant branch stars, and RSGs.

(e.g., Chen et al. 2010; Xu et al. 2022; Reichardt Chu et al. 2024). Reichardt Chu et al. (2022) argue that these power-law indexes are indicative of energy-driven outflows, where the energy is mostly conserved as outflows break out of the ISM and propagate into the CGM (see also Chen et al. 2010; Li et al. 2017; Kim et al. 2020).

Observationally, outflows have been measured largely based on stacking spectra from galaxies with similar physical properties to maximize spectral signal-to-noise ratios (e.g., Chen et al. 2010), or collecting a sufficient sample with one sight line per galaxy to cover a wide parameter space (e.g., Xu et al. 2022). While these approaches provide invaluable information on outflows over galactic scales, it remains unclear how outflows interact with their ambient environments on smaller scales. From theoretical perspectives, how outflows are generated and propagated in realistic environments such as the solar neighborhood and varying star formation conditions have been an active area of research (e.g., Li et al. 2017; Kim & Ostriker 2018; Kim et al. 2020; Andersson et al. 2023; Tan & Fielding 2023); however, these simulations remain largely unconstrained because of the scarcity of observational details on sub-kiloparsec scales.

In this work, we examine how varying star-forming conditions impact the physical properties of ionized outflows in the Large Magellanic Cloud (LMC). The LMC is the closest galaxy that hosts many bright H II regions, which makes it an ideal site to study how star formation drives outflows. Active star-forming regions are found across the LMC, such as 30 Doradus (30 Dor), N11, N44, N55, and N206 (Ambrocio-Cruz et al. 2016; McLeod et al. 2019). Table 1 lists the key physical parameters of the LMC, and Figure 1 illustrates the location

and movement of the present-day LMC with respect to the Milky Way (MW). At a distance of 50.1 kpc (Freedman et al. 2001) and moving in the MW halo at a Galactocentric velocity of 321 km s^{-1} (Kallivayalil et al. 2013), the LMC experiences strong headwinds due to ram pressure, which results in a truncated H I disk (Salem et al. 2015) and a potential bow shock leading the LMC (Setton et al. 2023).

Gas inflows and outflows have been detected using down-the-barrel observations toward individual massive stars bright in the UV in nearby galaxies (e.g., Howk et al. 2002; Danforth et al. 2002; Lehner & Howk 2007; Zheng et al. 2017). For the LMC, Wakker et al. (1998) detected C IV absorption with velocities offset from the galaxy's Hα emission using five stars observed with the Goddard High-Resolution Spectrograph on the Hubble Space Telescope (HST), which they interpreted as evidence for a hot halo around the LMC. Barger et al. (2016) compared ion absorption toward a pair of an LMC star and a background QSO that are $\sim$100 pc in projected separation; while the star only probes outflows in front of the LMC, the QSO sight line shows nearly symmetrical ion absorption due to outflows from both sides of the galaxy.

Thanks to the HST's Ultraviolet Legacy Library of Young Stars as Essential Standards (ULLYSES[12]) program (Roman-Duval et al. 2020), we are now able to probe the LMC's outflows on sub-kiloparsec scales using over a hundred UV sight lines (see Figure 2). This manuscript is the first in a series in which we investigate how the interplay between ram pressure and stellar feedback affects the kinematics and ionization structures of outflows and inflows in the LMC (#HST-AR-16640, PI: Zheng[13]).

This paper is organized as follows. In Section 2, we describe the ULLYSES LMC data set and relevant spectral analyses. In Section 3, we introduce auxiliary data sets in Hα, H I, and a sample of red supergiant stars (RSGs) to trace the LMC's recent star formation, and neutral and stellar disk kinematics. We show the main results in Section 4, and compare the LMC's outflows with those detected in starburst galaxies in Section 5. We also compare the observations with outflow simulation predictions in Section 5. We discuss the implications of our work in Section 6 and conclude in Section 7.

We release our data products, including normalized S II, Si IV, and C IV lines and their corresponding best-fit continuum models (when available), as a High Level Science Product called "LMC-FLOWS" at the Barbara A. Mikulski Archive for Space Telescopes (MAST).[14] Details on the UV data reduction can be found in Section 2.

Throughout this paper, the velocity is given in a heliocentric frame, unless otherwise specified. Toward the direction of the LMC, the heliocentric velocity v_{helio} and a velocity defined in the local standard of rest (LSR) is generally offset by $v_{helio} - v_{LSR} \sim 10$ km s^{-1}. We note that outflow velocities are typically measured in two ways in the literature: centroid velocities tracing bulk outflow mass (e.g., Heckman et al. 2015), or maximum velocities tracing terminal velocities of low-density outflowing gas (e.g., Chisholm et al. 2015). In this work, we adopt the first definition to describe the kinematic properties of bulk outflows in the LMC, $v_{out, bulk}$, unless otherwise specified.

---

[12] https://ullyses.stsci.edu/
[13] https://www.stsci.edu/cgi-bin/get-proposal-info?id=16640&observatory=HST
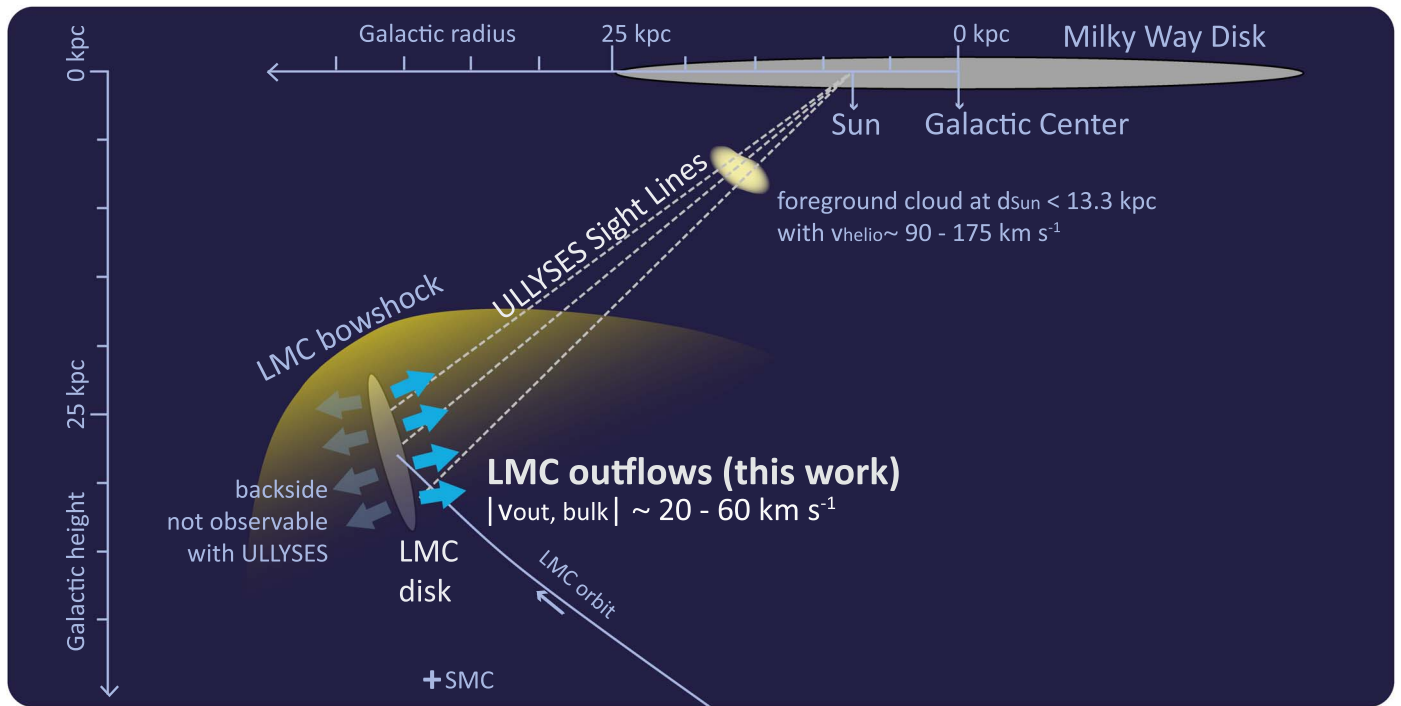[14] doi:10.17909/hz0m-np43

Figure 1. A schematic illustration of the present-day LMC with respect to the MW disk. The locations, orientations, and sizes of the LMC (star-forming) disk and a potential bow shock are based on a hydrodynamic simulation of the LMC orbiting in the MW halo (Setton et al. 2023, see their Figure 4); the simulation assumes the LMC to be on its first infall (Besla et al. 2007). The location of the Small Magellanic Cloud (SMC) is indicated as a cross. We highlight in blue arrows the LMC's outflows on its nearside, which we study in this work using 110 sight lines from the ULLYSES DR5. We also show the location of a foreground high-velocity cloud at $d_\odot < 13.3$ kpc (Richter et al. 2015; Werner & Rauch 2015), which contaminates potential LMC outflow absorption over $v_{\rm helio} \sim 90$–175 km s^{-1}. Our work focuses on the LMC gas at $v_{\rm helio} = 175$–375 km s^{-1} to minimize foreground contamination.

2. Data: UV Absorption

2.1. ULLYSES DR5 Sample Information

We use far-UV spectra of 110 massive stars in the LMC that were made public in the ULLYSES's fifth data release (DR5; 2022 June 28[15]; Roman-Duval et al. 2020). Figure 2 shows the distribution of the ULLYSES DR5 stellar sight lines in the LMC against background images of H I 21 cm (Kim et al. 2003) and Hα maps (Gaustad et al. 2001).

We are interested in those ULLYSES targets that were observed with the G130M and G160M gratings of the Cosmic Origins Spectrograph (COS), and/or the E140M grating of the Space Telescope Imaging Spectrograph (STIS). The COS data have spectral resolutions of $R = 12{,}000$–16,000 ($\delta v \approx 19$–25 km s^{-1}) in G130M and $R = 13{,}000$–20,000 in G160M ($\delta v \approx 15$–23 km s^{-1}) (COS Instrument Handbook, Soderblom 2023), and the STIS E140M data have a spectral resolution of $R = 45{,}800$ ($\delta v \approx 6.6$ km s^{-1}) (STIS Instrument Handbook, Medallon & Welty 2023). While the STIS data have a higher spectral resolution, the COS data offer a better sensitivity; this essentially means that STIS was used to observe bright stars while COS was targeted at fainter stars.

We use the coadded spectra released by the ULLYSES program and refer the reader to Roman-Duval et al. (2020) and the ULLYSES's data release page (see footnote 12) for more information. When available, we prioritize data taken with the STIS/E140M grating for the higher spectral resolution. We do not consider data taken with other gratings such as STIS/E140H or COS/G140L, which are less common among the ULLYSES targets; the only exception to this is the S II and Si

IV measurements toward star SK-67D83, which has both COS/G130M and STIS/E140H data, we use the STIS/E140H spectrum for its higher resolution ($R = 114{,}000$ or $\delta v \approx 2.6$ km s^{-1}). By design, both the STIS and COS data from the ULLYSES program yield a continuum signal-to-noise ratio of 20–30 per resolution element.

2.2. Far-UV Line Choices: S II, Si IV, and C IV Lines

There are a number of far-UV ions that are typically used to study gas flows in nearby galaxies, such as Si II, Si III, Si IV, C IV, and O VI (e.g., Wakker et al. 1998; Howk et al. 2002; Lehner & Howk 2007; Chisholm et al. 2015, 2016; Barger et al. 2016; Zheng et al. 2017). We focus on the Si IV 1393/1402 Å and C IV 1548/1550 Å doublets in the LMC. We choose Si IV and C IV because they are relatively less saturated than Si II and Si III in the LMC, and thus provide a more accurate characterization of the gas kinematics. Si IV and C IV trace a cool-warm-ionized phase with $T \sim 10^{4\text{-}5}$ K, which is found to contain most of the mass in an outflow in hydrodynamic simulations of feedback-driven outflows (e.g., Li et al. 2017; Kim et al. 2020; Rathjen et al. 2021).

Although a large fraction of the ULLYSES sight lines also have O VI 1031/1037 Å spectra from the Far Ultraviolet Spectroscopic Explorer (FUSE), we do not use O VI in this work because the O VI 1037 Å line is in a region with multiple contaminants, and the O VI 1031 Å is complicated due to the broad interstellar O VI absorption blended with stellar wind features with unknown continuum shapes. The O VI 1031 Å line is also contaminated by H_2 absorption (see Howk et al. 2002).

The Si IV and C IV doublets are in spectral regions with no other contaminating ISM lines. But, one of the main challenges
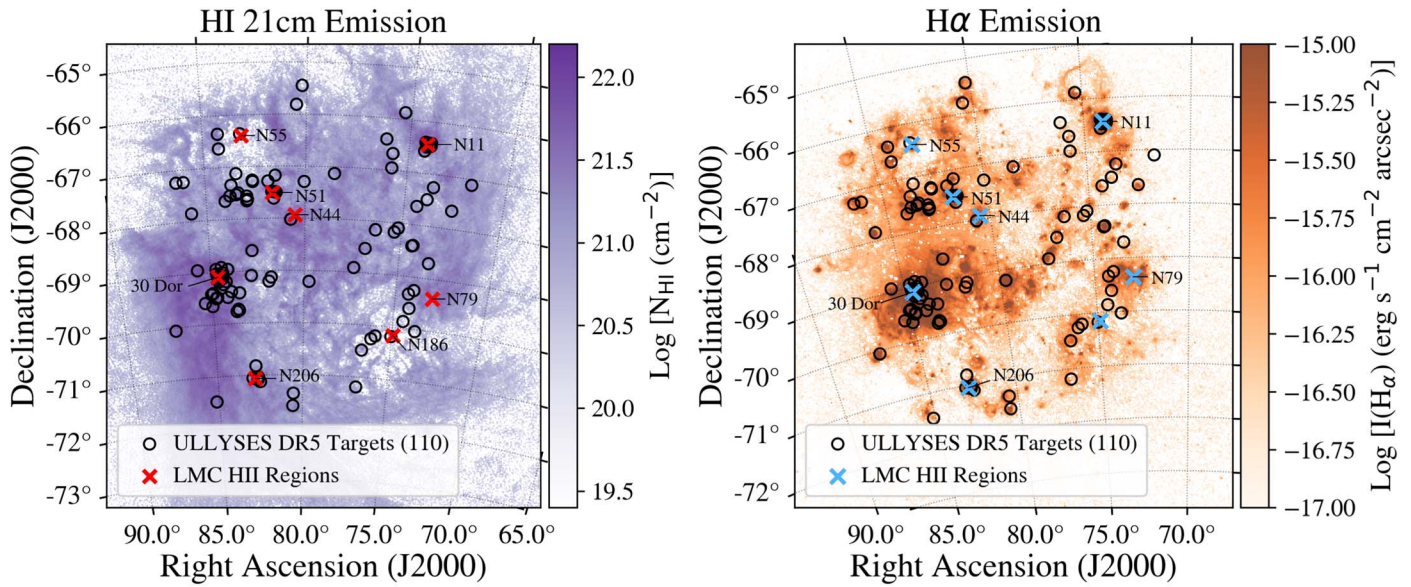

Figure 2. Distribution of 110 ULLYSES DR5 stellar sight lines (black circles) across the LMC. The left panel shows an H I column density map (Kim et al. 2003) and the right panel shows a continuum-subtracted Hα intensity map of the LMC (Gaustad et al. 2001). Red and blue crosses in the left and right panels indicate several major H II regions in the LMC, respectively. We introduce the ULLYSES data set in Section 2, and the H I and Hα data sets in Section 3.
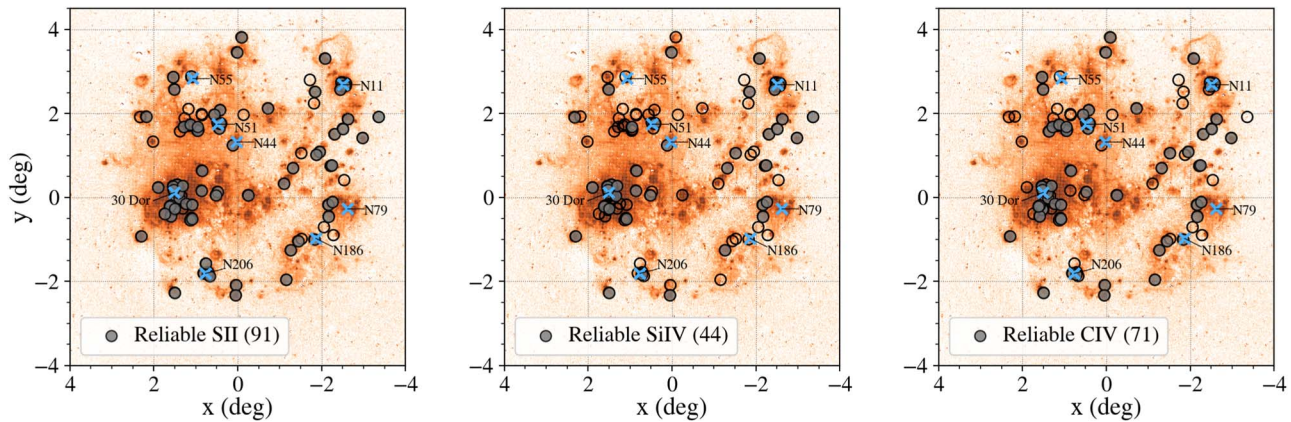

Figure 3. Distribution of the ULLYSES sight lines against the Hα map in an orthographic projection in the LMC plane, following the method outlined in Choi et al. (2022). At the distance of the LMC (50.1 kpc) (Freedman et al. 2001), 1 deg ≈0.9 kpc. Major H II regions are indicated by blue crosses. Gray-filled circles indicate those sight lines with reliable S II (91/110; left), Si IV (44/110; middle), and C IV (71/109; right) measurements over the LMC's absorption range of $v_{\rm helio} = 175\text{--}375$ km s^{-1}. An ion measurement is considered reliable if (1) its stellar continuum shows a strong P Cygni profile such that the LMC's interstellar absorption can be reliably identified, and (2) the column density difference between doublet lines is within what is allowed by the apparent optical depth method (Savage & Sembach 1991, 1996). See Section 2 for further details.

in analyzing Si IV and C IV is that the widths of the stellar absorption lines are, for some stars in the sample, comparable to the widths of the interstellar absorption lines along the LMC's lines of sight. In the next section, we develop an evaluation matrix to select stars with smooth continua that allow accurate stellar continuum modeling over the almost 500 km s^{-1} range spanned by interstellar absorption from the MW, intervening halo gas, and the LMC.

We also analyze S II 1250/1253 Å lines that trace a less ionized phase of the LMC's ISM. We do not use the S II 1259 Å line because it is blended with Si II 1260 Å from the MW's ISM. In Figure 3, we show in filled circles the ULLYSES sight lines with reliable S II (91/110), Si IV (44/110), and C IV (71/109[16]) measurements for the LMC's interstellar absorption; we describe how we determine reliable

ion measurements in the following sections. The atomic data, including accurate wavelengths and oscillator strengths, are adopted from Morton (2003).

2.3. Selection of Stars with Well-developed P Cygni Profiles in Si IV or C IV

Among the 110 LMC stars in the ULLYSES DR5, there are 57 O-type stars, 28 B-type stars, 15 Wolf–Rayet stars, and 10 with other types such as binaries or luminous blue variables.[17] The key to extracting reliable Si IV and C IV interstellar

---

[16] There are only 109 stars with C IV coverage; star SK-66D17 was only observed with COS/G130M in ULLYSES DR5.

[17] Three stars are labeled either as an O-type or a Wolf–Rayet star, including LMCe055-1 (WN4/O4), SK-67D22 (O2If*/WN5), and VFTS-482 (O2.5 If*/WN6); for a classification purpose, we group them under the Wolf–Rayet category. Two binaries, HD38029 (WC4+OB) and SK-69D246 (WN5/6h +WN6/7h), are also grouped under the Wolf–Rayet category, in which one or both of the stars are Wolf–Rayet type. The category classification does not significantly affect the results shown in this work.

absorption lines is to identify OB stellar spectra with well-developed P Cygni profiles (Savage & de Boer 1981; Howk et al. 2002). The P Cygni profiles often take the form of redshifted emission peaks with optically thick, blueshifted absorption troughs due to absorption and subsequent reemission of photons in stellar winds (Kudritzki & Puls 2000).

We only consider ULLYSES stars that meet the following criteria: (1) the stars have developed winds/P Cygni profiles in Si IV or C IV, (2) the winds have *high optical depths* such that the fluxes of the absorption troughs are low or approaching zero, and (3) the winds have *high terminal velocities* such that the blue edges of the troughs are far from line centers.

Criterion 1 excludes stars with stellar absorption that may have similar widths to the MW and LMC interstellar absorption. Criterion 2 excludes stars with complex spectral shapes because it is difficult to accurately model pseudo-continua over the interstellar absorption regions for P Cygni profiles with low optical depths. Lastly, we implement criterion 3, excluding winds with low terminal velocities, because a large fraction of a narrow P Cygni profile will contain interstellar absorption.

In the left panels of Figure 4, we show three examples of Si IV line profiles that meet criteria 1–3. In the right panels, we show another three examples where the stars have either no recognizable Si IV winds (top right), low opacity winds (middle right), or low terminal velocity winds that cause sharp rising profiles (bottom right). We note that the Si IV and C IV spectra of the 15 Wolf–Rayet stars are generally dominated by broad stellar features that can be easily distinguished from interstellar absorption, so we use these Wolf–Rayet stars without considering criteria 1–3.

To apply criteria 1–3 quantitatively, we develop an automated algorithm based on a general observation that stronger stellar winds with high opacities result in deeper blueshifted absorption troughs where the fluxes approach zero (e.g., Hawcroft et al. 2023). We define a *wind ratio* parameter, f_w, which is the depth of a blue absorption trough with respect to the height of a red emission peak. In practice, f_w is computed as the ratio of the median flux over $v_{helio} = [-400, -100]$ km s^{-1} in the rest frame of the bluer line (Si IV 1393 or C IV 1548) to the median flux over $v_{helio} = [475, 775]$ km s^{-1} in the rest frame of the redder line (Si IV 1402 or C IV 1550). In Figure 4, we highlight these two flux regions in blue and red vertical shades, respectively.

The reasoning for the f_w parameterization is as follows. We do not use the ratio of the minimum absorption to the maximum emission fluxes because this is only applicable to spectra that have developed P Cygni profiles. For those without obvious P Cygni profiles (e.g., top right panel of Figure 4), the locations of the minimum and maximum fluxes are subject to local spectral variations, and in many cases, the MW/LMC lines are the strongest absorption features. Second, stellar winds with high terminal velocities will have blended Si IV or C IV profiles instead of distinct peaks and troughs; this is best seen in star SK-69D50 (bottom left in Figure 4) where the red peak of Si IV 1393 is absorbed by the blue trough of Si IV 1402. Lastly, we measure a median absorption flux over $[-400, -100]$ km s^{-1} blueward of the bluer lines to avoid the MW's ISM absorption near ∼0 km s^{-1}; similarly, we measure a median emission flux over $[475, 775]$ km s^{-1} redward of the redder lines to avoid the LMC's interstellar absorption. The 300 km s^{-1} velocity interval reduces the impact of noise, local spectral variations, and differences in wind terminal velocities.

We examine a set of Si IV and C IV P Cygni profiles of OB stars from the Potsdam Wolf–Rayet models (Hainich et al. 2019)

at the LMC's metallicity and determine that a threshold at

$$f_w = \frac{\langle I_{blue} \rangle}{\langle I_{red} \rangle} \leqslant 0.6 \qquad (1)$$

can best provide an adequate diagnostic to select stars with well-developed winds. The number of stars that pass the threshold only changes by less than 10 when we vary the f_w threshold by ±0.1. For C IV, Equation (1) is analogous to the "good" or "best" quality scores set by Hawcroft et al. (2023) when estimating C IV terminal velocities for 67 OB stars in the ULLYSES LMC data set, where the minimum flux of the blue absorption trough is roughly less than half of the continuum average. In Section 2.5, we will use Equation (1) to select stars with reliable interstellar absorption in Si IV and C IV.

2.4. Continuum Fitting, Ion Column Densities, and Centroid Velocities

We describe our continuum-fitting algorithm using the Si IV doublet in Figure 4 as an example, and note that the same procedure is applied to S II and C IV. For Si IV and C IV, the continuum fitting is performed for every star independent of its spectral type or wind ratio f_w (Equation (1)).

For each ion doublet, we select a spectral region that covers ∼5–10 Å blueward of the bluer line and ∼5–10 Å redward of the redder line.[18] We mask a velocity range[19] of $v_{helio} \sim [-100, 380]$ km s^{-1} at the rest frame of each line to cover both the MW and LMC interstellar absorption. To predict stellar continuum over the masked velocity region, a typical approach is to fit low-order Legendre polynomials to absorption-free regions near the lines of interest (e.g., Howk et al. 2002; Lehner & Howk 2007; Lehner et al. 2009; Barger et al. 2016; Zheng et al. 2017). However, as shown in Figure 4, the stellar continuum is highly variable from star to star and from line to line. To automate the fitting process and reduce human biases in the continuum placement, we developed a continuum-fitting algorithm based on the concept of Gaussian process regression (Rasmussen & Williams 2006) and the open-source package George[20] (Ambikasaran et al. 2015).

Instead of assuming a particular function form (e.g., polynomials), Gaussian process is a nonparametric process that models the probabilistic distributions of all available model functions. We refer to the unmasked part of the Si IV stellar continuum (free of interstellar absorption) as the training set X and the masked velocity region where we want to predict stellar continuum shape as the test set Y. The first step of a Gaussian process is to estimate the probability distribution function of the training set, $\mathcal{N}(\mu_X, \Sigma_X)$, where μ_X is the sample mean and Σ_X is a covariance matrix that describes the correlation of every spectral point x_i with itself and every other spectral point in X. We estimate the covariance matrix Σ_X by applying a kernel function to model the training set X that takes the form of either a squared exponential kernel or a Matern 3/2 kernel. We then use the scipy.minimize function to fit

---

[18] The exact width of the spectral region does not matter as long as it covers the doublet interstellar absorption and provides enough stellar continuum as a training set for the Gaussian process.

[19] Because COS's line-spread function is broader and less well-defined than STIS's, interstellar absorption lines in COS appear to be ∼30–50 km s^{-1} broader than those in STIS. For this reason, the velocity mask for each line is determined by visual inspection, and the mask chosen for a COS absorption line is generally ∼50 km s^{-1} wider than that of STIS.

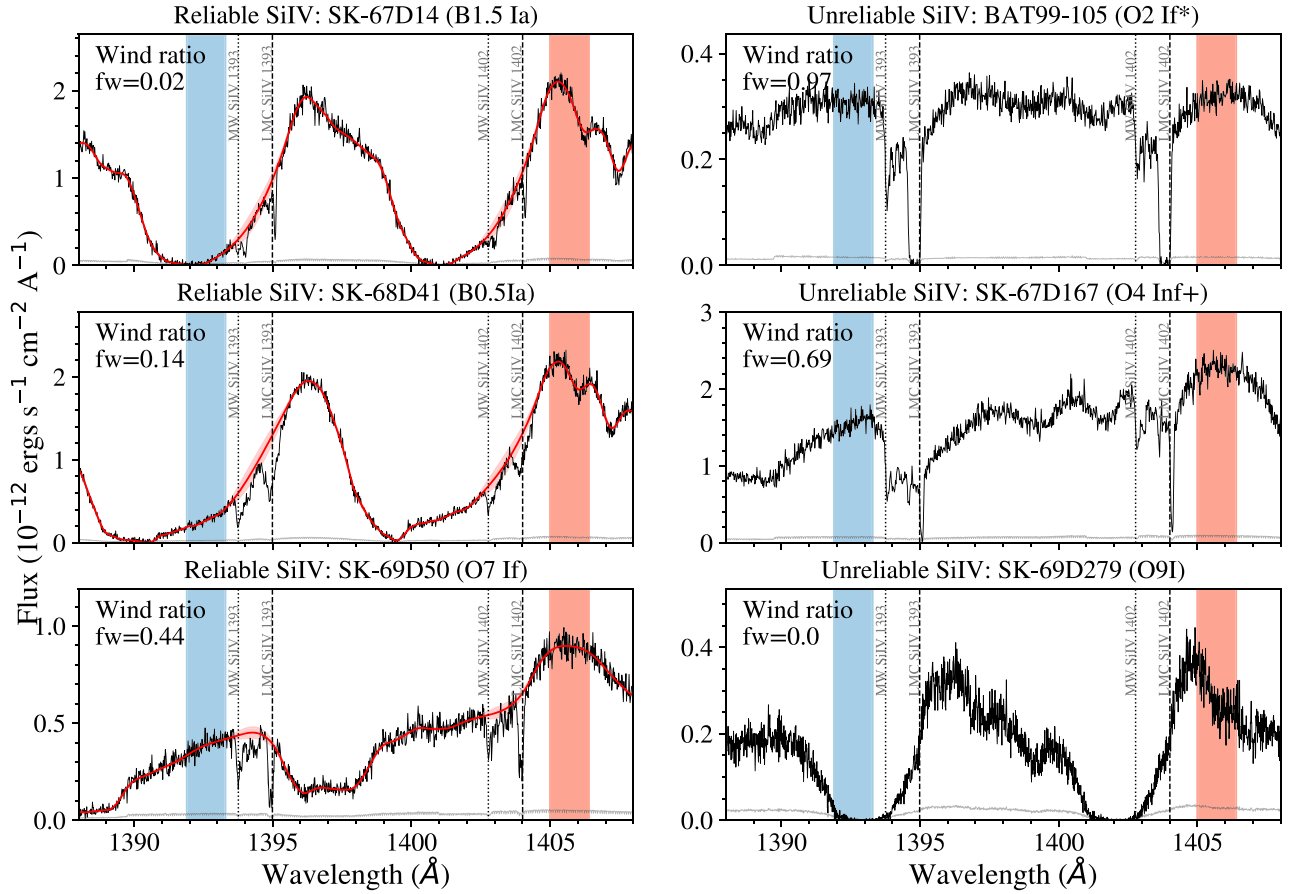[20] https://george.readthedocs.io/en/latest/

Figure 4. Left: example spectra with well-developed P Cygni profiles in Si IV (see Section 2.3), with fluxes in black curves and errors in gray. The MW and LMC Si IV absorption can be reliably separated from the stellar P Cygni profiles. We show in red curves the best-fit continuum models, which we discuss in Section 2.4. Right: example spectra that have either mild or no stellar winds, in which case the Si IV absorption from stellar photospheres blends heavily with the MW and LMC interstellar absorption; we consider these Si IV unreliable. In each panel, the blue and red vertical shades indicate the stellar continuum regions that we use to calculate the wind ratios f_w (Equation (1)) to quantify the strengths of stellar winds/P Cygni profiles.

for the maximum likelihood parameters for the kernel function and use that to predict the stellar continuum shape over the test set Y (i.e., the masked velocity region).

In the left panels of Figure 4 where three examples of reliable Si IV interstellar absorption are shown, we plot the best-fit continua as red curves with 1σ uncertainties. We divide the fluxes by the best-fit continua to normalize each doublet's lines. The uncertainties of the normalized fluxes have combined the original flux errors and the continuum-fitting uncertainties through error propagation.

We calculate ion column densities based on the apparent optical depth method (AOD; Savage & Sembach 1991, 1996). The AOD method can also be used to test whether a stellar continuum is placed correctly, which we describe as follows. For an ion line with normalized fluxes of $I_n(v)$,[21] its apparent column density as a function of velocity is

$$N_a(v) = 3.768 \times 10^{14} \frac{\tau_a(v)}{f\lambda(\text{Å})} \ [\text{cm}^{-2} \ (\text{km s}^{-1})^{-1}]$$

$$N_a = \int_{v_{min}}^{v_{max}} N_a(v) dv, \quad (2)$$

where f is the oscillator strength, λ the rest wavelength in units of angstrom, and $\tau_a(v)$ the apparent optical depth smeared by an instrumental broadening profile.

We adopt a fixed velocity range of $[v_{min}, v_{max}] = [175, 375] \text{ km s}^{-1}$ to measure the integrated ion column densities of the LMC. The left bound is chosen to avoid contamination from a foreground high-velocity cloud (HVC) at $v \sim 90$–175 km s^{-1} within 13.3 kpc from the Sun (see Figure 1; Lehner et al. 2009; Richter et al. 2015; Werner & Rauch 2015; Roman-Duval et al. 2019). And the right bound is chosen such that the integration range is wide enough to cover the entire LMC absorption. Figure 5 shows two examples where in one case (left panel) the absorption from the foreground HVC and the LMC can be clearly distinguished near $v = 175 \text{ km s}^{-1}$, while in the other case (right panel) the two structures blend mildly together near $v = 175 \text{ km s}^{-1}$.

We quantify whether the HVC and the LMC absorption are well separated by measuring the mean absorption flux of an ion line (S II 1253, Si IV 1393, C IV 1548) over a velocity range of $v = 175 \pm 5 \text{ km s}^{-1}$. If the mean flux is more than 80% of the continuum flux, such as the case in the left panels of Figure 5, we consider the line to have well-separated HVC and LMC absorption. We check all reliable S II, Si IV, and C IV normalized lines and confirm that along most sight lines (82/91 for S II, 34/44 for Si IV, and 49/71 for C IV), the HVC and LMC absorption can be well separated at $\sim 175 \text{ km s}^{-1}$—the

---

[21] For some STIS spectra from the ULLYSES DR5, when a line is saturated, the fluxes near the line center appear to be lower than the errors at the same velocities. In this case, we replace those fluxes with the corresponding error values in the AOD calculation.
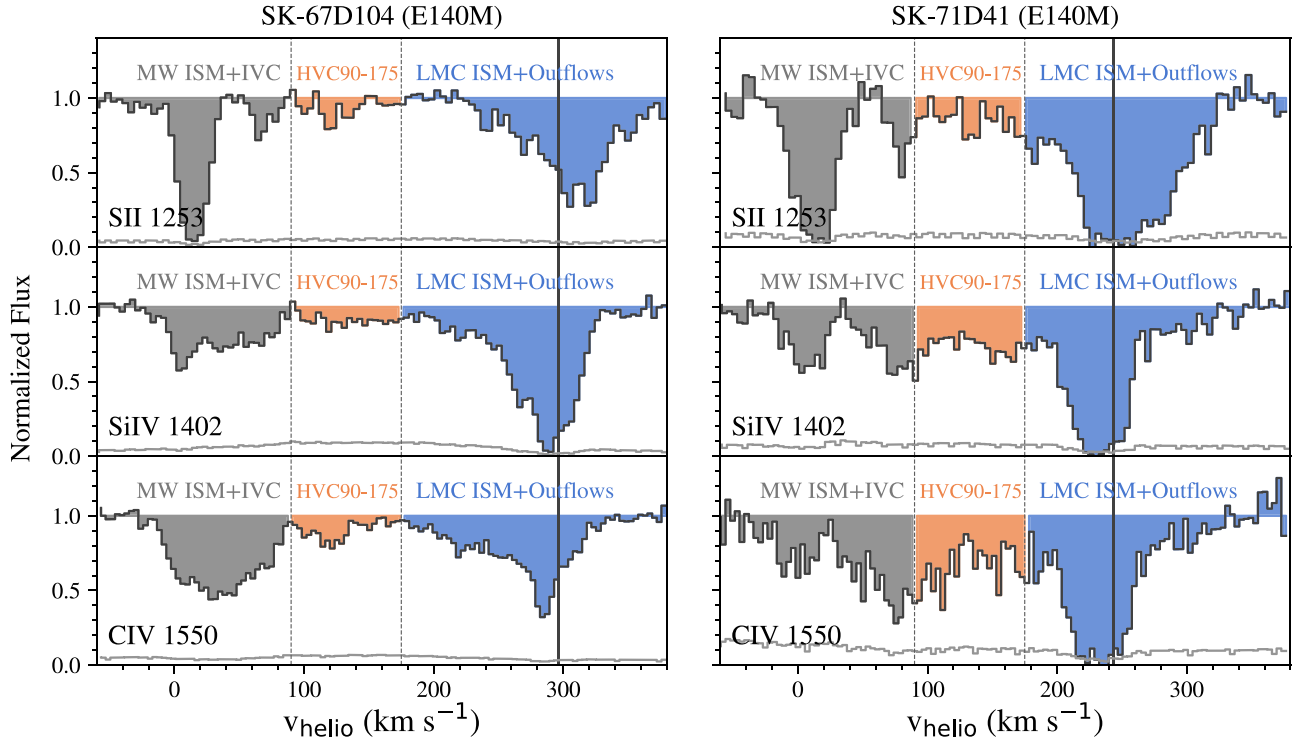
Figure 5. Normalized S II, Si IV, and C IV spectra for SK-67D104 (left) and SK-71D41 (right). We highlight three velocity components: (1) the MW's ISM and intermediate velocity cloud at $v \lesssim 90$ km s^{-1} (gray), (2) a high-velocity cloud at $90 \lesssim v \lesssim 175$ km s^{-1} and $d_\odot < 13.3$ kpc in the foreground (HVC90-175 (orange)), and (3) the LMC's ISM and outflows at $175 \lesssim v \lesssim 375$ km s^{-1} (blue). The relative spatial locations of the three components are sketched in Figure 1. The solid vertical lines show the velocities of the LMC's stellar disk at the locations of the stars (see Section 3). The left panel shows an example sight line where the absorption from HVC90-175 and the LMC (ISM+outflows) can be well separated near $v = 175$ km s^{-1}, while the right panel shows an example where the two components are blended. We quantify the degree of blending between HVC90-175 and the LMC absorption near $v = 175$ km s^{-1} in Section 2.4.

spectra shown in the left panels are more common. Thus, setting v_{min} at 175 km s^{-1} minimizes contamination from the foreground HVC.

The S II, Si IV, and C IV doublets all have a doublet ratio of $f_1 \lambda_1/f_2 \lambda_2 = 2$, where the subscript 1 is for the stronger line and 2 for the weaker line. This means the integrated column density ratio of an ion doublet is

$$\frac{N_{2,a}}{N_{1,a}} = \frac{[\int \tau_{2,a}(v) dv]/f_2 \lambda_2}{[\int \tau_{1,a}(v) dv]/f_1 \lambda_1} = \frac{\int \tau_{2,a}(v) dv}{\int \tau_{1,a}(v) dv} \times 2. \quad (3)$$

In cases where both lines of a doublet are fully resolved without saturation, we expect $N_{1,a} = N_{2,a}$ and the column density difference between the doublet lines to be $\Delta \log_{10} N \equiv \log_{10} N_{2,a} - \log_{10} N_{1,a} = 0$. On the other hand, when both lines are fully saturated with normalized fluxes near zero, we expect $\int \tau_{1,a}(v) dv \approx \int \tau_{2,a}(v) dv$, and the column density difference between the doublet lines to be $N_{2,a}/N_{1,a} \approx 2$ or $\Delta \log_{10} N \approx 0.3$ dex (Savage & Sembach 1991; Jenkins 1996). Therefore, for lines that are moderately saturated, the column density difference between the doublet lines should be

$$-\sigma_N \leqslant \Delta \log_{10} N \leqslant +\sigma_N + 0.3 \text{ dex}, \quad (4)$$

where σ_N is the uncertainty tolerance set by the quadratic sum of the uncertainties in $N_{1,a}$ and $N_{2,a}$. In Section 2.5, we will combine Equation (4) with the wind ratio threshold in Equation (1) to select stars with reliable interstellar absorption in S II, Si IV, and C IV.

We compute each line's centroid velocity weighted by the apparent optical depth over the same velocity range. The uncertainty on the centroid velocity is calculated by propagating the errors in the apparent optical depth array over the same velocity range, which are computed based on the continuum-normalized flux errors. Our centroid velocity calculation is similar to the weighted average velocity used in Chisholm et al. (2015, 2016), which traces the bulk motion of outflowing gas. While Chisholm et al. (2015, 2016) show that v_{90}, velocity at 90% of the continuum flux level, can trace low-density gas and thus probe the terminal velocity of outflows (of the corresponding transition lines), we do not compute v_{90} because of potential contamination from the foreground HVC at $\sim$90–175 km s^{-1} toward some sight lines (see Figure 5). We discuss the physical properties of this HVC in Section 6.4.

2.5. Summary of Selection Rules and Final Target List

We adopt two criteria to evaluate whether a best-fit continuum produces reliable S II, Si IV, or C IV interstellar absorption lines: (1) whether we expect a star to have a smooth continuum as a result of being a Wolf–Rayet star or having $f_w \leqslant 0.6$ (Equation (1), Section 2.3), and (2) whether the column density differences of the normalized ion doublet's lines are within theoretical values specified in Equation (4) (Section 2.4). Note that criterion 1 is only applied to Si IV and C IV to distinguish narrow ISM lines from broad P Cygni profiles due to massive stars' stellar winds.

In total, we identify 71 ULLYSES stars (out of 109) with reliable C IV continuum placement over the LMC's absorption range, 44/110 with reliable Si IV, and 91/110 with reliable S

II. The spatial distribution of these reliable ion measurements across the LMC is shown in Figure 3. We tabulate each ion's integrated column density and centroid velocity in Table 2.

Figure 6 shows the distribution of selected stars as a function of spectral type. Most stars with reliable interstellar C IV absorption are Wolf–Rayet, O types, or B types earlier than B1, and most stars with reliable interstellar Si IV are Wolf–Rayet, O types later than O6, or B types earlier than B2. There are only 44 stars in Si IV passing our selection rules because most of the early O-type stars are with winds that are highly ionized and thus with no significant Si IV P Cygni profiles; the lack of winds results in Si IV stellar features spanning over similar wavelength widths as the MW and LMC interstellar absorption, such as the top right panel of Figure 4. In such cases, our algorithm flags the stars as having unreliable Si IV. For S II, the only rule that is used to select reliable interstellar absorption is whether the $\Delta \log_{10} N$ condition in Equation (4) is satisfied. So, the distribution in the S II panel does not show a particular trend with spectral types, and most (91/110) stars have reliable S II continuum placement.

3. Auxiliary Data Sets: Hα, H I, and RSGs

We supplement the ULLYSES DR5 sample with three additional data sets to estimate the LMC's SFR surface density (Σ_{SFR}; Section 3.1), the total column density and bulk velocity of neutral hydrogen (H I; Section 3.2), and the LMC's stellar disk kinematics (Section 3.3). The derived Σ_{SFR}, H I column densities and centroid velocities, and line-of-sight stellar disk velocities are tabulated in Table 2.

3.1. Hα Emission from the Southern Hα Sky Survey Atlas

We obtained a continuum-subtracted Hα emission map of the LMC from the Southern Hα Sky Survey Atlas (SHASSA; Gaustad et al. 2001). The survey has a filter width of 32 Å and covers a spatial range of decl. $\sim (-90°, +15°)$ at a resolution of $\approx 0.'8$ and with a sensitivity of 2R or 1.2×10^{-17} ergs cm^{-2} s^{-1} arcsec^{-2}. The Hα map has been corrected for flux contribution from the [N II] 6549/6585 doublet lines that fall within the filter (see Section 4 in Gaustad et al. 2001). Considering the LMC's metallicity and the SHASSA's filter width, the Hα emission traces star formation activities happening within the last ~ 7–10 Myr (Haydon et al. 2020). We calculate the LMC's Σ_{SFR} values as follows.

We first convert the observed Hα intensity $I(\text{H}\alpha)$ to Hα luminosity as $L_{\text{obs}}(\text{H}\alpha) = 4\pi D^2 \theta^2 I(\text{H}\alpha)$, where $D = 50.1$ kpc (Freedman et al. 2001) and θ is the angular size of the region of interest in units of arcsec. We factor in the inclination of the LMC and calculate $L_{\text{obs}}(\text{H}\alpha)$ for every 0.1×0.1 kpc^2 deprojected area in the LMC; the region size of 0.1×0.1 kpc^2 is to ensure sufficient sampling of the initial mass function such that the following luminosity to SFR relation holds (Kennicutt & Evans 2012). We adopt 8% uncertainties in Hα fluxes (Gaustad et al. 2001) and propagate the errors in the following calculation.

To correct for dust attenuation, we first use a stellar reddening map from red clump stars by Choi et al. (2018) and calculate $E(B-V)_{\text{star}}$ values for 108 out of the 110 ULLYSES stellar sight lines. For the remaining two sight lines outside the Choi et al. map, SK-65D47 and SK-65D55, we obtain $E(B-V)_{\text{star}}$ values from Skowron et al. (2021), which agrees well with Choi et al. around the main star-forming disk. We then estimate the corresponding nebular gas reddening

values as $E(B-V)_{\text{gas}} = E(B-V)_{\text{star}}/0.44$ following the relation from Calzetti (1997).

To evaluate gas reddening uncertainties, we compare our $E(B-V)_{\text{gas}}$ values with those available from Balmer decrement measurements using integral field unit observations of H II regions by Lah et al. (2024). For 31 ULLYSES sight lines that are within <100 pc of Lah et al.'s H II regions, we find that our $E(B-V)_{\text{gas}}$ values agree well with theirs with a median offset of $\sim 15\%$. We thus adopt a uniform error of 15% in $E(B-V)_{\text{gas}}$ for all our ULLYSES sight lines and propagate the errors in the following calculation.

Lastly, we compute the Hα extinction values $A_{\text{H}\alpha}$ using the LMC's average extinction curve (Gordon et al. 2003) and derive the intrinsic Hα luminosity as $L_{\text{int}}(\text{H}\alpha) = L_{\text{obs}}(\text{H}\alpha)/10^{(-0.4 A_{\text{H}\alpha})}$. We convert each region's $L_{\text{int}}(\text{H}\alpha)$ to SFR as $\log_{10} \text{SFR} = \log_{10} L_{\text{int}}(\text{H}\alpha) - 41.27$, following the formulation in Kennicutt & Evans (2012), which assumes an initial mass function from Kroupa & Weidner (2003). The SFR surface density Σ_{SFR} is estimated by dividing the SFR value of each region by the corresponding size of 0.1×0.1 kpc^2, yielding a unit of $M_\odot$ yr^{-1} kpc^{-2}.

Figure 7 shows the distribution of the ULLYSES DR5 sight lines as a function of Σ_{SFR}. A majority of the sight lines are in regions with $\Sigma_{\text{SFR}} \sim 10^{-2}$–$1 M_\odot$ yr^{-1} kpc^{-2}, with a handful of sight lines directly probing either 30 Dor or other H II regions (see Figures 2 and 3). The clustering of the sight lines near major H II regions ultimately affects the range of outflow environments that we will probe, which we discuss in Section 4. We note that our spectral analyses algorithm does not exacerbate the sampling bias—Figure 7 shows that the histogram distributions of reliable S II, Si IV, and C IV measurements are consistent with the distributions of the original ULLYSES data set.

3.2. H I 21 cm Dataset

The H I data cube is a combination of an interferometry observation with the Australia Telescope Compact Array at 1′ resolution (Kim et al. 1998), and a single-dish observation with the Parkes multibeam receiver at 16.'9 (Kim et al. 2003). The combined data cube has a spatial resolution of 1′, a spectral resolution of 1.6 km s^{-1}, and a flux sensitivity of $\sigma_T \sim 2.4$ K (or ~ 15 mJy beam^{-1}), and it spans a velocity range from 190 to 386 km s^{-1} in the heliocentric frame.

For each ULLYSES DR5 sight line, we extract median H I fluxes of all spatial pixels within a diameter of 1 beam (1′) of the sight line. We then integrate the H I spectrum over its entire velocity range to obtain an estimate of the H I column density $N_{\text{H I}}$. The centroid velocity v_c is estimated as the flux-weighted velocity over pixels in the spectrum with fluxes higher than $2\sigma_T$. The flux threshold here is to ensure that the centroid velocity of each spectrum reflects the kinematics of the majority of bright (dense) H I gas along a line of sight. We find that this method better traces the center of mass for the H I gas than the velocity estimated at a peak flux, especially in cases where there are multiple H I velocity components toward some LMC regions (Kim et al. 2003; Oh et al. 2022).

We note that there are five sight lines with negative H I fluxes from the combined data cube that indicate self-absorption: VFTS440, BAT99-105, VFTS-482, SK-65D47, and SK-67D266. For these sight lines, we do not attempt to estimate the total $N_{\text{H I}}$ or centroid velocities, and note "self-abs" in the corresponding entries in Table 2. Additionally, there are

Table 2
Column Density and Velocity Measurements of the LMC Gas along the ULLYSES DR5 Sight Lines

ID	Star	R.A. (deg)	Decl. (deg)	x (deg)	y (deg)	$\log \Sigma_{\rm SFR}$ ($M_\odot$ yr^{-1} kpc^{-2})	$v_{\rm RSG}$ (km s^{-1})	$\log N$(H I) (cm^{-2})	$v_{\rm HI}$ (km s^{-1})	$\log N$(S II) (cm^{-2})	$v_{\rm cen}$(S II) (km s^{-1})	$\log N$(Si IV) (cm^{-2})	$v_{\rm cen}$(Si IV) (km s^{-1})	$\log N$(C IV) (cm^{-2})	$v_{\rm cen}$(C IV) (km s^{-1})
(1)	(2)	(3)	(4)	(5)	(6)	(7)	(8)	(9)	(10)	(11)	(12)	(13)	(14)	(15)	(16)
1	SK-68D73	80.7491	−68.0296	0.11	1.24	−0.916 ± 0.052	288.5	21.57	291.2	>15.77	294.1 ± 25.6	>13.93	268.0 ± 14.4	Unreliable	Unreliable
2	BAT99-105	84.6755	−69.0987	1.51	0.12	0.194 ± 0.044	271.7	Self-abs	Self-abs	>16.21	260.8 ± 17.6	Unreliable	Unreliable	>14.93	228.7 ± 13.4
3	ST92-5-31	84.7985	−69.5104	1.52	−0.29	−0.597 ± 0.042	265.7	21.65	273.6	>15.83	268.9 ± 5.8	Unreliable	Unreliable	>14.37	242.4 ± 5.4
4	SK-67D22	74.3644	−67.6508	−2.31	1.51	−2.063 ± 0.055	284.7	21.21	284.9	>15.46	283.3 ± 13.5	>13.62	310.9 ± 23.7	13.80 ± 0.02	293.1 ± 22.7
5	SK-66D172	84.2725	−66.3597	1.53	2.86	−1.189 ± 0.057	302.5	21.27	301.9	>15.73	287.0 ± 15.8	Unreliable	Unreliable	>14.35	291.0 ± 26.9
6	VFTS72	84.3936	−69.0195	1.41	0.21	−0.573 ± 0.048	273.0	21.59	275.5	>15.78	277.0 ± 8.8	Unreliable	Unreliable	>14.90	244.1 ± 5.5
7	BI237	84.0610	−67.6553	1.37	1.58	−1.458 ± 0.054	292.7	21.47	292.0	Unreliable	Unreliable	Unreliable	Unreliable	>14.57	285.4 ± 9.2
8	SK-67D211	83.8079	−67.5576	1.28	1.68	−0.581 ± 0.042	294.2	21.27	296.9	>15.68	288.8 ± 24.3	Unreliable	Unreliable	>14.71	283.0 ± 24.0
9	VFTS-482	84.6679	−69.0999	1.51	0.12	0.194 ± 0.044	271.7	Self-abs	Self-abs	>16.06	269.6 ± 3.5	>14.41	222.2 ± 3.4	Unreliable	Unreliable
10	N11-ELS-060	74.1756	−66.4152	−2.50	2.73	−0.398 ± 0.056	288.3	21.36	290.9	>15.73	264.2 ± 5.8	Unreliable	Unreliable	Unreliable	Unreliable
11	ST92-5-27	84.8065	−69.5014	1.53	−0.28	−0.579 ± 0.042	265.8	21.63	273.2	>15.85	264.8 ± 6.1	Unreliable	Unreliable	>14.55	239.6 ± 7.6
12	LH114-7	85.8042	−67.8544	2.02	1.33	−1.287 ± 0.055	288.9	21.30	301.6	Unreliable	Unreliable	Unreliable	Unreliable	Unreliable	Unreliable
13	VFTS-267	84.5582	−69.1299	1.46	0.09	0.164 ± 0.048	271.3	21.65	279.6	>15.86	272.0 ± 11.7	Unreliable	Unreliable	>14.44	231.7 ± 9.5
14	VFTS-404	84.6410	−69.1659	1.49	0.06	−0.043 ± 0.045	270.7	21.62	278.0	>16.00	274.5 ± 11.0	Unreliable	Unreliable	>14.71	236.0 ± 7.5
15	W61-28-23	83.7090	−69.7757	1.13	−0.53	−1.101 ± 0.039	262.3	21.28	273.6	>15.63	265.8 ± 10.5	Unreliable	Unreliable	>14.21	248.2 ± 12.4
16	SK-71D46	82.9566	−71.0606	0.82	−1.80	−0.875 ± 0.049	243.7	21.51	245.9	>15.62	256.8 ± 9.4	Unreliable	Unreliable	13.96 ± 0.02	229.5 ± 11.7
17	SK-67D166	82.9342	−67.6337	0.95	1.62	−1.290 ± 0.054	293.7	20.82	294.2	15.13 ± 0.01	261.8 ± 7.7	Unreliable	Unreliable	13.67 ± 0.02	263.7 ± 14.1
18	SK-67D105	81.5258	−67.1824	0.42	2.09	−1.449 ± 0.056	300.6	21.03	308.4	>15.22	303.7 ± 28.4	Unreliable	Unreliable	13.87 ± 0.03	271.6 ± 24.6
19	SK-67D108	81.6103	−67.6223	0.44	1.65	−1.141 ± 0.055	294.2	21.31	296.1	>15.45	286.8 ± 10.6	Unreliable	Unreliable	>14.23	275.6 ± 8.4
20	HD38029	84.2299	−69.1938	1.34	0.04	−0.580 ± 0.045	270.6	21.69	277.0	Unreliable	Unreliable	13.61 ± 0.04	238.2 ± 32.2	Unreliable	Unreliable
21	SK-67D167	82.9663	−67.6615	0.96	1.59	−0.962 ± 0.054	293.3	21.24	296.8	15.22 ± 0.01	278.2 ± 12.3	Unreliable	Unreliable	>14.02	259.4 ± 20.6
22	W61-28-5	83.6186	−69.7325	1.10	−0.49	−1.203 ± 0.039	262.9	21.03	267.4	Unreliable	Unreliable	Unreliable	Unreliable	>14.46	253.4 ± 7.6
23	FARINA-88	85.0343	−69.6548	1.59	−0.44	−0.552 ± 0.042	263.4	21.68	265.0	>15.98	258.6 ± 5.0	Unreliable	Unreliable	>14.46	234.6 ± 5.1
24	LMCE055-1	74.2034	−69.6113	−2.17	−0.45	−2.163 ± 0.050	262.9	20.94	268.2	15.51 ± 0.02	233.4 ± 14.4	>14.01	234.6 ± 10.5	>14.40	228.9 ± 7.1
25	SK-70D60	76.1699	−70.2596	−1.44	−1.04	−2.200 ± 0.048	255.4	20.39	242.3	14.77 ± 0.03	239.6 ± 26.8	Unreliable	Unreliable	13.82 ± 0.03	216.6 ± 25.4
26	SK-65D47	80.2280	−65.4550	−0.09	3.81	−1.846 ± 0.063	304.5	Self-abs	Self-abs	15.38 ± 0.02	261.3 ± 14.0	Unreliable	Unreliable	14.02 ± 0.02	268.2 ± 17.6
27	SK-67D69	78.5837	−67.1342	−0.72	2.13	−2.004 ± 0.051	301.5	21.25	303.2	>15.72	289.9 ± 14.8	Unreliable	Unreliable	>14.23	270.0 ± 11.4
28	VFTS352	84.6186	−69.1886	1.48	0.03	−0.169 ± 0.045	270.4	21.70	277.7	>15.78	275.5 ± 5.0	Unreliable	Unreliable	Unreliable	Unreliable
29	ST92-4-18	84.9612	−69.4076	1.59	−0.19	−0.800 ± 0.042	267.1	21.57	272.6	>15.89	274.9 ± 6.5	Unreliable	Unreliable	13.79 ± 0.02	221.9 ± 13.7
30	N11-ELS-038	74.1884	−66.4197	−2.50	2.72	−0.400 ± 0.056	288.3	21.34	286.5	>15.55	287.3 ± 12.7	Unreliable	Unreliable	>14.16	269.4 ± 13.5
31	PGMW3120	74.1951	−66.4130	−2.50	2.73	−0.398 ± 0.056	288.4	21.39	290.4	>15.86	279.7 ± 28.0	Unreliable	Unreliable	>14.52	274.1 ± 23.9
32	LMCE078-1	84.3734	−69.2478	1.39	−0.02	−0.649 ± 0.045	269.7	21.67	277.2	>15.81	283.1 ± 11.9	Unreliable	Unreliable	>14.28	256.1 ± 12.5
33	SK-65D22	75.3462	−65.8759	−2.08	3.31	−1.672 ± 0.054	293.5	21.04	294.9	>15.72	278.3 ± 18.6	>13.66	274.1 ± 16.0	13.95 ± 0.02	273.0 ± 22.4
34	SK-71D19	80.5656	−71.3609	0.04	−2.09	−2.089 ± 0.050	239.7	20.96	242.3	>15.51	240.5 ± 14.8	Unreliable	Unreliable	14.26 ± 0.02	250.2 ± 14.3
35	SK-69D104	79.7479	−69.2152	−0.25	0.06	−0.757 ± 0.049	271.2	21.19	276.7	15.10 ± 0.01	260.6 ± 11.9	Unreliable	Unreliable	13.62 ± 0.05	215.5 ± 36.0
36	VFTS440	84.6572	−69.0892	1.50	0.13	0.189 ± 0.044	271.9	Self-abs	Self-abs	>15.90	274.0 ± 44.2	Unreliable	Unreliable	>14.64	224.0 ± 27.7
37	N11-ELS-018	74.1710	−66.4113	−2.50	2.73	−0.433 ± 0.056	288.3	21.43	292.2	>15.62	275.5 ± 9.9	Unreliable	Unreliable	>14.12	264.3 ± 11.9
38	UCAC3-42-30814	83.9660	−69.3886	1.24	−0.15	−1.084 ± 0.040	267.8	21.08	269.1	>15.64	271.7 ± 10.7	Unreliable	Unreliable	>14.46	254.6 ± 4.7
39	SK-67D111	81.7003	−67.4916	0.48	1.78	−0.828 ± 0.056	296.1	21.19	301.7	>15.47	293.0 ± 14.4	13.50 ± 0.03	256.6 ± 22.4	13.77 ± 0.03	260.6 ± 28.0
40	SK-71D50	85.1799	−71.4835	1.50	−2.27	−2.345 ± 0.048	243.4	21.45	254.7	>15.90	264.2 ± 20.6	13.48 ± 0.04	233.0 ± 32.4	13.56 ± 0.08	249.5 ± 69.2
41	SK-70D115	87.2069	−70.0661	2.30	−0.92	−0.895 ± 0.051	259.7	21.55	257.0	>15.90	277.6 ± 8.4	>14.20	239.2 ± 19.0	>14.40	238.4 ± 17.3
42	BI214	83.5258	−69.4193	1.08	−0.17	−1.496 ± 0.040	267.6	21.07	272.4	>15.80	267.7 ± 19.6	Unreliable	Unreliable	>14.48	242.9 ± 7.9
43	SK-66D19	73.9748	−66.4165	−2.58	2.72	−1.032 ± 0.054	287.5	21.50	289.0	>15.39	256.3 ± 31.3	13.77 ± 0.03	274.8 ± 27.3	14.00 ± 0.04	256.8 ± 33.4
44	BI272	86.0963	−67.2414	2.18	1.93	−1.812 ± 0.057	295.4	20.73	310.0	>15.55	287.5 ± 10.3	Unreliable	Unreliable	Unreliable	Unreliable
45	SK-69D50	74.3129	−69.3389	−2.16	−0.17	−1.991 ± 0.051	266.9	20.79	271.5	>15.48	243.0 ± 20.3	>13.64	249.0 ± 21.7	13.90 ± 0.04	249.4 ± 35.0

Table 2
(Continued)

ID	Star	R.A. (deg)	Decl. (deg)	x (deg)	y (deg)	$\log \Sigma_{SFR}$ ($M_\odot$ yr^{-1} kpc^{-2})	v_{RSG} (km s^{-1})	$\log N$(H I) (cm^{-2})	v_{HI} (km s^{-1})	$\log N$(S II) (cm^{-2})	v_{cen}(S II) (km s^{-1})	$\log N$(Si IV) (cm^{-2})	v_{cen}(Si IV) (km s^{-1})	$\log N$(C IV) (cm^{-2})	v_{cen}(C IV) (km s^{-1})
46	SK-68D16	74.4075	−68.4100	−2.22	0.75	−0.949 ± 0.053	278.8	20.85	284.7	>15.47	267.6 ± 10.0	Unreliable	Unreliable	13.94 ± 0.02	235.4 ± 18.4
47	SK-67D118	81.8888	−67.2918	0.56	1.97	−1.850 ± 0.056	299.0	20.96	318.1	15.21 ± 0.02	269.5 ± 15.7	Unreliable	Unreliable	14.03 ± 0.03	272.9 ± 24.1
48	UCAC3-42-33014	85.0568	−69.4264	1.62	−0.22	−0.873 ± 0.042	266.8	21.35	277.0	>15.79	273.7 ± 9.2	>14.42	221.4 ± 6.6	>14.81	218.9 ± 4.8
49	SK-68D112	82.7835	−68.6151	0.85	0.64	−1.348 ± 0.052	279.5	21.46	276.4	15.42 ± 0.01	270.3 ± 11.3	>13.69	233.8 ± 8.8	13.66 ± 0.03	223.8 ± 26.6
50	SK-67D191	83.3918	−67.5055	1.13	1.74	−1.343 ± 0.053	295.3	21.39	297.1	>15.60	285.9 ± 14.1	Unreliable	Unreliable	>14.52	276.6 ± 19.2
51	SK-68D155	85.7289	−68.9485	1.90	0.24	−1.436 ± 0.048	273.4	21.76	280.5	>15.86	288.5 ± 12.5	13.85 ± 0.02	241.5 ± 13.0	Unreliable	Unreliable
52	N11-ELS-013	74.2536	−66.4070	−2.47	2.74	−0.375 ± 0.056	288.6	21.59	295.2	>15.83	274.7 ± 29.0	Unreliable	Unreliable	>14.42	275.5 ± 32.5
53	BI173	81.7915	−69.1323	0.48	0.13	−1.737 ± 0.049	272.2	21.07	249.8	>15.75	235.0 ± 11.0	Unreliable	Unreliable	13.85 ± 0.04	224.4 ± 29.5
54	SK-67D101	81.4844	−67.5080	0.40	1.76	−0.801 ± 0.056	295.9	21.26	301.6	15.36 ± 0.02	293.3 ± 19.1	Unreliable	Unreliable	14.03 ± 0.02	263.9 ± 19.5
55	SK-67D168	82.9672	−67.5724	0.96	1.68	−1.709 ± 0.054	294.6	<20.4	N/A	15.17 ± 0.01	257.2 ± 12.4	13.35 ± 0.02	249.4 ± 15.5	13.52 ± 0.06	246.2 ± 44.8
56	LMCX-4	83.2065	−66.3703	1.11	2.88	−1.763 ± 0.056	302.9	<20.4	N/A	14.71 ± 0.03	264.2 ± 25.7	Unreliable	Unreliable	Unreliable	Unreliable
57	BI184	82.6278	−71.0421	0.71	−1.78	−0.992 ± 0.047	244.0	20.94	262.0	>15.61	261.5 ± 6.0	Unreliable	Unreliable	Unreliable	Unreliable
58	LH9-34	74.1887	−66.4936	−2.49	2.65	−0.756 ± 0.056	288.2	21.40	278.3	>15.95	269.2 ± 23.8	13.45 ± 0.01	250.3 ± 10.5	13.88 ± 0.03	245.8 ± 25.9
59	SK-71D8	76.8469	−71.1983	−1.16	−1.96	−2.159 ± 0.052	243.8	20.87	228.9	>15.89	223.2 ± 18.6	Unreliable	Unreliable	14.23 ± 0.02	232.0 ± 16.7
60	VFTS-66	84.3879	−69.0762	1.41	0.15	−0.162 ± 0.048	272.2	21.72	275.3	>15.83	273.4 ± 13.1	Unreliable	Unreliable	Unreliable	Unreliable
61	SK-66D171	84.2601	−66.6436	1.51	2.58	−1.559 ± 0.055	300.9	21.16	315.8	>15.57	267.3 ± 12.7	13.33 ± 0.02	254.8 ± 17.1	13.72 ± 0.05	255.0 ± 41.3
62	SK-69D279	85.4361	−69.5875	1.74	−0.39	−1.412 ± 0.043	264.2	21.57	270.7	>15.77	267.3 ± 14.3	Unreliable	Unreliable	Unreliable	Unreliable
63	SK-70D32	75.0425	−70.1860	−1.83	−0.99	−1.714 ± 0.049	256.0	20.96	246.4	15.17 ± 0.02	226.6 ± 18.8	Unreliable	Unreliable	13.65 ± 0.05	203.0 ± 41.0
64	SK-66D17	73.9812	−66.4724	−2.57	2.66	−1.104 ± 0.054	287.4	21.30	280.6	>15.64	271.2 ± 10.3	Unreliable	Unreliable	N/A	N/A
65	SK-68D135	84.4548	−68.9171	1.44	0.31	−0.997 ± 0.051	274.5	21.55	278.3	>15.89	274.4 ± 17.9	>14.36	255.3 ± 16.6	Unreliable	Unreliable
66	VFTS87	84.4027	−69.1255	1.41	0.10	−0.112 ± 0.048	271.5	21.77	277.0	>15.79	271.8 ± 44.9	Unreliable	Unreliable	>14.30	248.9 ± 38.2
67	SK-71D41	82.6673	−71.0936	0.72	−1.83	−0.931 ± 0.048	243.2	21.39	246.9	>15.82	247.9 ± 23.5	>14.21	235.6 ± 19.6	>14.60	233.6 ± 20.7
68	SK-67D5	72.5789	−67.6606	−2.98	1.42	−1.718 ± 0.057	276.4	21.20	280.0	>15.56	272.6 ± 12.4	13.25 ± 0.03	256.5 ± 27.0	13.56 ± 0.05	239.2 ± 43.7
69	SK-69D220	84.1820	−69.4965	1.31	−0.26	−1.224 ± 0.039	266.2	21.35	285.5	Unreliable	Unreliable	Unreliable	Unreliable	Unreliable	Unreliable
70	SK-68D52	76.8351	−68.5357	−1.32	0.70	−1.854 ± 0.051	280.8	21.23	254.1	>15.75	264.2 ± 14.0	13.71 ± 0.02	240.0 ± 15.2	14.20 ± 0.02	242.6 ± 13.9
71	SK-67D107	81.5862	−67.4988	0.44	1.77	−0.805 ± 0.056	296.1	21.25	305.0	15.38 ± 0.02	283.7 ± 16.7	>14.20	284.2 ± 21.0	>14.31	280.5 ± 16.2
72	SK-67D106	81.5634	−67.5000	0.43	1.77	−0.791 ± 0.056	296.1	21.23	306.4	15.36 ± 0.02	295.0 ± 18.6	>14.16	274.4 ± 23.1	>14.22	268.9 ± 16.6
73	HV5622	77.3717	−68.9174	−1.10	0.33	−0.903 ± 0.051	275.4	21.30	266.6	>15.68	258.9 ± 8.6	Unreliable	Unreliable	Unreliable	Unreliable
74	N11-ELS-033	74.0459	−66.4734	−2.55	2.66	−0.883 ± 0.054	287.6	21.25	279.6	>15.65	271.3 ± 6.7	13.62 ± 0.01	245.8 ± 12.1	Unreliable	Unreliable
75	SK-70D79	76.6553	−70.4901	−1.26	−1.26	−1.829 ± 0.049	252.1	21.11	241.4	>15.62	226.8 ± 19.5	>13.58	209.8 ± 19.4	>14.09	211.9 ± 18.5
76	SK-69D43	74.0436	−69.2606	−2.26	−0.11	−2.183 ± 0.051	267.1	20.74	264.1	15.22 ± 0.02	234.6 ± 15.8	13.52 ± 0.01	253.2 ± 10.7	13.70 ± 0.04	243.1 ± 30.2
77	SK-68D41	76.3630	−68.1674	−1.52	1.05	−1.770 ± 0.050	286.0	21.33	267.6	Unreliable	Unreliable	13.59 ± 0.02	257.2 ± 12.5	13.94 ± 0.03	249.2 ± 25.5
78	SK-68D140	84.7382	−68.9481	1.54	0.27	−0.708 ± 0.046	273.9	21.68	275.4	>15.73	277.2 ± 18.4	>14.33	251.0 ± 14.5	>14.58	250.6 ± 3.4
79	SK-67D2	71.7686	−67.1148	−3.36	1.92	−3.191 ± 0.054	275.5	21.30	273.2	>15.72	272.6 ± 20.8	13.67 ± 0.02	254.5 ± 14.2	Unreliable	Unreliable
80	SK-68D23A	75.2012	−68.0996	−1.95	1.09	−2.361 ± 0.055	285.5	21.19	267.3	15.45 ± 0.01	259.3 ± 9.9	Unreliable	Unreliable	14.16 ± 0.02	238.1 ± 14.2
81	SK-66D35	74.2685	−66.5774	−2.45	2.57	−0.981 ± 0.057	288.3	21.51	287.7	>15.79	261.7 ± 16.1	13.57 ± 0.02	258.4 ± 14.4	Unreliable	Unreliable
82	SK-68D129	84.1116	−68.9589	1.32	0.27	−1.100 ± 0.050	274.1	21.54	278.4	>15.61	266.4 ± 13.5	>14.02	251.2 ± 9.9	>14.44	245.0 ± 4.0
83	N206-FS-170	82.7622	−70.8323	0.76	−1.57	−2.805 ± 0.046	247.1	21.16	248.4	15.33 ± 0.03	254.1 ± 22.3	Unreliable	Unreliable	Unreliable	Unreliable
84	SK-71D35	82.5174	−71.1323	0.67	−1.87	−1.242 ± 0.048	242.7	21.29	245.7	>15.55	247.8 ± 10.0	Unreliable	Unreliable	Unreliable	Unreliable
85	NGC1818-ROB-D1	76.1346	−66.4132	−1.72	2.80	−2.790 ± 0.056	295.6	21.27	302.4	Unreliable	Unreliable	Unreliable	Unreliable	Unreliable	Unreliable
86	SK-67D14	73.6329	−67.2568	−2.63	1.87	−1.657 ± 0.059	283.3	21.24	291.1	>15.42	255.3 ± 14.8	13.35 ± 0.05	276.8 ± 46.2	>14.08	262.3 ± 17.5
87	SK-69D52	74.4538	−69.8729	−2.06	−0.70	−2.651 ± 0.050	259.6	20.56	258.8	Unreliable	Unreliable	Unreliable	Unreliable	Unreliable	Unreliable
88	SK-68D26	75.3844	−68.1786	−1.88	1.02	−2.200 ± 0.054	285.5	21.24	269.2	>15.79	267.7 ± 11.4	Unreliable	Unreliable	Unreliable	Unreliable
89	NGC2004-ELS-26	82.6515	−67.2952	0.85	1.96	−2.189 ± 0.056	298.4	20.98	308.7	Unreliable	Unreliable	Unreliable	Unreliable	Unreliable	Unreliable

Table 2
(Continued)

ID	Star	R.A. (deg)	Decl. (deg)	x (deg)	y (deg)	$\log \Sigma_{SFR}$ ($M_\odot$ yr^{-1} kpc^{-2})	v_{RSG} (km s^{-1})	$\log N$(H I) (cm^{-2})	v_{HI} (km s^{-1})	$\log N$(S II) (cm^{-2})	v_{cen}(S II) (km s^{-1})	$\log N$(Si IV) (cm^{-2})	v_{cen}(Si IV) (km s^{-1})	$\log N$(C IV) (cm^{-2})	v_{cen}(C IV) (km s^{-1})
90	SK-70D50	75.9412	−70.1993	−1.52	−0.98	−2.171 ± 0.051	256.2	20.64	245.7	Unreliable	Unreliable	Unreliable	Unreliable	Unreliable	Unreliable
91	SK-67D78	80.0795	−67.3016	−0.14	1.97	−2.455 ± 0.054	299.1	21.00	297.8	Unreliable	Unreliable	Unreliable	Unreliable	Unreliable	Unreliable
92	SK-69D140	81.9141	−69.2116	0.52	0.05	−1.834 ± 0.049	271.1	20.73	267.6	15.35 ± 0.02	224.2 ± 15.8	13.33 ± 0.03	249.4 ± 27.1	Unreliable	Unreliable
93	SK-70D16	73.7390	−70.0412	−2.28	−0.89	−2.234 ± 0.051	256.2	20.51	244.5	Unreliable	Unreliable	Unreliable	Unreliable	Unreliable	Unreliable
94	SK-68D8	73.4304	−68.7148	−2.54	0.41	−2.592 ± 0.052	271.5	20.88	266.6	Unreliable	Unreliable	Unreliable	Unreliable	Unreliable	Unreliable
95	NGC2004-ELS-3	82.6684	−67.2691	0.86	1.99	−2.218 ± 0.056	298.5	21.09	307.8	Unreliable	Unreliable	Unreliable	Unreliable	Unreliable	Unreliable
96	SK-67D195	83.4664	−67.1339	1.17	2.11	−2.460 ± 0.055	298.2	20.47	292.3	Unreliable	Unreliable	Unreliable	Unreliable	Unreliable	Unreliable
97	SK-67D197	83.4961	−67.5377	1.17	1.71	−1.438 ± 0.053	294.8	21.24	299.1	Unreliable	Unreliable	Unreliable	Unreliable	Unreliable	Unreliable
98	SK-66D50	75.7868	−66.9597	−1.82	2.24	−2.447 ± 0.055	293.6	21.16	286.3	Unreliable	Unreliable	Unreliable	Unreliable	Unreliable	Unreliable
99	SK-67D207	83.7311	−67.3519	1.27	1.89	−1.717 ± 0.055	296.2	20.74	302.8	Unreliable	Unreliable	Unreliable	Unreliable	Unreliable	Unreliable
100	SK-67D20	73.8806	−67.5007	−2.51	1.64	−2.409 ± 0.058	283.2	20.70	283.5	15.09 ± 0.05	262.7 ± 41.5	>13.79	274.5 ± 20.2	>14.41	269.2 ± 25.0
101	SK-68D15	74.3504	−68.3992	−2.24	0.76	−0.936 ± 0.053	278.7	21.01	285.8	15.43 ± 0.02	267.4 ± 14.1	>14.00	241.1 ± 16.9	13.98 ± 0.01	230.7 ± 10.4
102	SK-66D51	75.7871	−66.6826	−1.84	2.52	−2.240 ± 0.055	294.1	20.46	299.8	>15.27	292.8 ± 25.9	>13.69	267.5 ± 14.2	Unreliable	Unreliable
103	SK-65D55	80.4904	−65.8167	0.02	3.45	−1.937 ± 0.063	304.3	<20.4	N/A	14.93 ± 0.03	253.4 ± 23.8	>13.54	272.7 ± 18.6	>14.10	271.6 ± 14.2
104	SK-71D21	80.5939	−71.5995	0.05	−2.33	−1.500 ± 0.049	238.3	21.18	247.0	>15.46	255.3 ± 16.2	13.39 ± 0.04	229.7 ± 35.0	13.72 ± 0.04	238.9 ± 33.3
105	SK-67D104	81.5165	−67.4992	0.41	1.77	−0.781 ± 0.056	296.1	21.18	302.4	15.26 ± 0.02	286.9 ± 21.3	>14.07	283.6 ± 10.4	>14.10	270.5 ± 11.1
106	SK-69D175	82.8563	−69.0940	0.86	0.16	−1.347 ± 0.049	272.6	21.05	275.3	>15.57	268.2 ± 14.5	13.23 ± 0.04	225.1 ± 32.3	Unreliable	Unreliable
107	SK-69D191	83.5802	−69.7529	1.09	−0.51	−1.188 ± 0.039	262.6	21.19	261.4	>15.84	255.6 ± 16.2	>13.97	253.1 ± 9.2	>14.36	249.1 ± 5.3
108	SK-69D246	84.7224	−69.0336	1.53	0.18	0.020 ± 0.044	272.7	21.65	275.6	>15.92	266.3 ± 20.2	>14.16	229.7 ± 16.3	>14.42	225.4 ± 9.4
109	HD269927C	84.7421	−69.4888	1.50	−0.27	−0.607 ± 0.042	266.0	21.61	276.6	>15.96	270.2 ± 19.7	>14.25	218.8 ± 15.4	Unreliable	Unreliable
110	SK-67D266	86.4664	−67.2405	2.33	1.92	−1.752 ± 0.059	295.4	Self-abs	Self-abs	Unreliable	Unreliable	>13.49	284.7 ± 41.7	Unreliable	Unreliable

Note. Columns (1)–(4): IDs, star names, R.A., and decl. of the targets from the ULLYSES program (DR5). Columns (5)–(6): x and y coordinates of each star in the plane of the LMC based on the orthographic projection method outlined in Choi et al. (2022). Column (7): star formation rate surface density measured toward each sight line based on an Hα emission map from Gaustad et al. (2001); see Section 3.1 for further details. Column (8): heliocentric velocities of the LMC's young stellar disk at the locations of the corresponding sight lines, measured based on the kinematic model of a population of young supergiant stars (RSGs); see Section 3.3 for further details. Columns (9)–(10): column densities and flux-weighted centroid velocities of the H I gas, measured based on an H I 21 cm data cube from Kim et al. (2003). We find H I self-absorption in five sight lines, BAT99-105 (ID 2), VFTS-482 (ID 9), SK-65D47 (ID 26), VFTS440 (ID 36), and SK-67D266 (ID 110), which we note as "Self-abs" in the corresponding entries. Additionally, we do not find significant H I detection along three sight lines, SK-67D168 (ID 55), LMCX-4 (ID 56), and SK-65D55 (ID 103), for which we indicate 3σ upper limits in log N(H I) based on the data cube's sensitivity level; see Section 3.2 for further details. Columns (11)–(16): column densities and centroid velocities of S II, Si IV, and C IV integrated from $v_{helio} = 175$ to 375 km s^{-1} based on the AOD method (see Section 2.4 for details). A measurement is labeled as "Unreliable" when our algorithm does not find a reliable continuum placement over the MW+LMC interstellar absorption velocity range; see Section 2.5 for further details. For each ion doublet, we use the weaker lines (S II 1250, Si IV 1402, C IV 1550) when the stronger lines are saturated. The only exception is Si IV measured toward SK-68D73, which only has STIS/E140H coverage extending up to Si IV 1393 Å but not 1402 Å; in this case, we use the measurement from Si IV −1393 Å. When both lines of an ion doublet are nonsaturated, we take the mean values of the doublet lines and the errors are combined in quadrature.

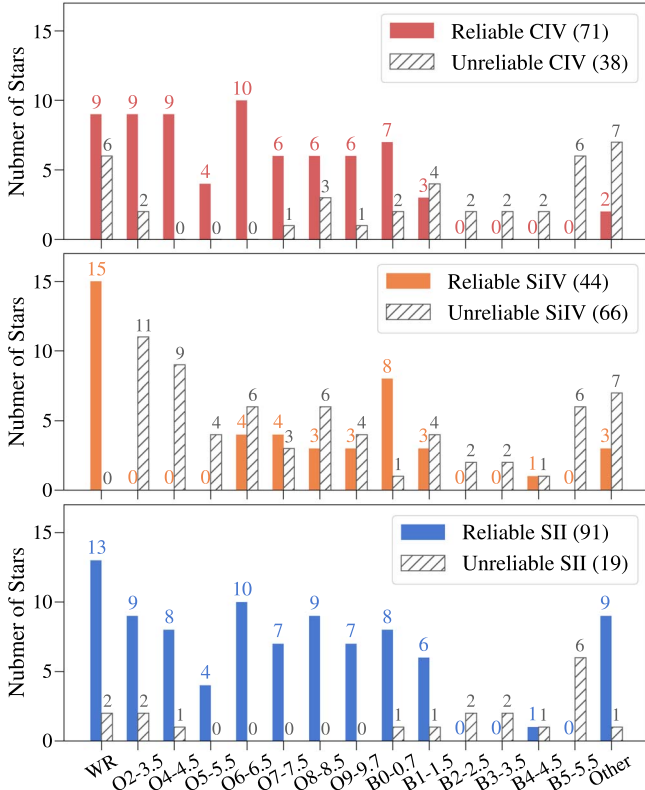(This table is available in machine-readable form in the online article.)

Figure 6. Distribution of stars with reliable C IV (top), Si IV (middle), and S II (bottom panel) LMC interstellar absorption as a function of spectral type. Those sight lines that we adopt in our LMC analysis (i.e., reliable) are shown in blue, red, and orange, respectively, and those that we consider unreliable and thus discarded are shown in gray. See discussion in Section 2.5.

three sight lines with low H I signals (S/N < 3); for these cases, we indicate 3σ upper limits in $N_{\mathrm{H\,I}}$, but do not obtain v_c.

3.3. Kinematics of the LMC's Young Stellar Disk from RSGs

We adopt a kinematic model of the LMC's stellar disk that is based on the line-of-sight heliocentric velocities of 738 RSGs analyzed by Olsen et al. (2011). This model includes the effects of the LMC's bulk center-of-mass motion and internal rotation on the observed line-of-sight velocities, as discussed by van der Marel et al. (2002). The RSGs represent a young ($\lesssim 20$ Myr) stellar disk, and their internal rotation curve is found to be consistent with that of the LMC's H I gas (Olsen et al. 2011).

At the locations of the ULLYSES DR5 sight lines, we calculate the line-of-sight velocities predicted by the RSG-based model; these are the velocities that stars would have at the corresponding locations if they resided in the LMC disk plane, shared the LMC's center-of-mass motion, and moved on circular orbits at speeds specified by the fitted rotation curve. We tabulate these model velocities as v_{RSG} in Table 2, and use v_{RSG} as the velocity reference of the LMC stellar disk to examine the relative motions of multiphase gas probed by H I, S II, Si IV, and C IV in the following sections.

4. Results

We discuss our main results, which compare the S II, Si IV, and C IV ion properties to other properties of the LMC such as the H I gas content, Σ_{SFR}, and stellar kinematics. The measurements of these properties are tabulated in Table 2. Specifically, we look into how the ionized gas kinematics is
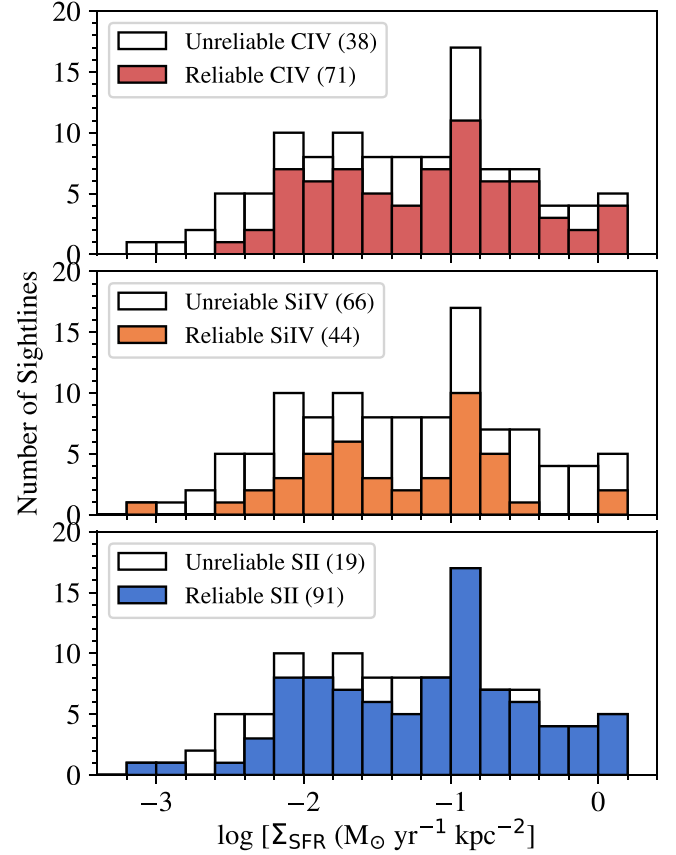
Figure 7. Histogram distributions of the ULLYSES DR5 sight lines as a function of Σ_{SFR} in logarithmic values. Sight lines with reliable C IV (top), Si IV (middle), and S II (bottom) are highlighted in blue, orange, and red, respectively.

blueshifted with respect to the H I and stellar disk kinematics, indicating the presence of disk-wide outflows.

4.1. Ion Column Density versus Σ_{SFR}

In the top panels of Figure 8, we show the column densities of H I, S II, Si IV, and C IV with respect to Σ_{SFR} toward each line of sight. H I and S II trace neutral and low ionization gas in the LMC's ISM, and Si IV and C IV trace warm-ionized gas at $T \sim 10^{4-5}$ K. In general, we find that the H I and ionized gas column densities all increase with Σ_{SFR} across the LMC disk.

For S II, Si IV, and C IV, the column density thresholds above which the ion lines become saturated (i.e., lower N limits) are around $\sim 10^{15.4}$ cm^{-2}, $\sim 10^{13.6}$ cm^{-2}, and $\sim 10^{14.0}$ cm^{-2}, respectively. The saturation rates increase toward regions with high Σ_{SFR}; in general, all ions are saturated (100%) at $\Sigma_{\mathrm{SFR}} \gtrsim 10^{-0.5} M_\odot$ yr^{-1} kpc^{-2}. We note that, by design, the ULLYSES sight lines are targeted at massive stars that reside in or near active star-forming regions (see Figure 3).

In the bottom panels of Figure 8, we show the two-dimensional (2D) distributions of H I, S II, Si IV, and C IV column densities across the LMC disk in the same orthographic projection as in Figure 3. We grid the S II, Si IV, and C IV data sets into $0°.5 \times 0°.5$ bins and calculate mean ion column densities of all sight lines within each bin. Most bins have one sight line per bin, and there are ~ 2–8 sight lines per bin for ~ 10 bins near major H II regions. For sight lines with lower-limit $\log N$ values, we treat the lower limits as detections when calculating the mean and place an upward arrow in the
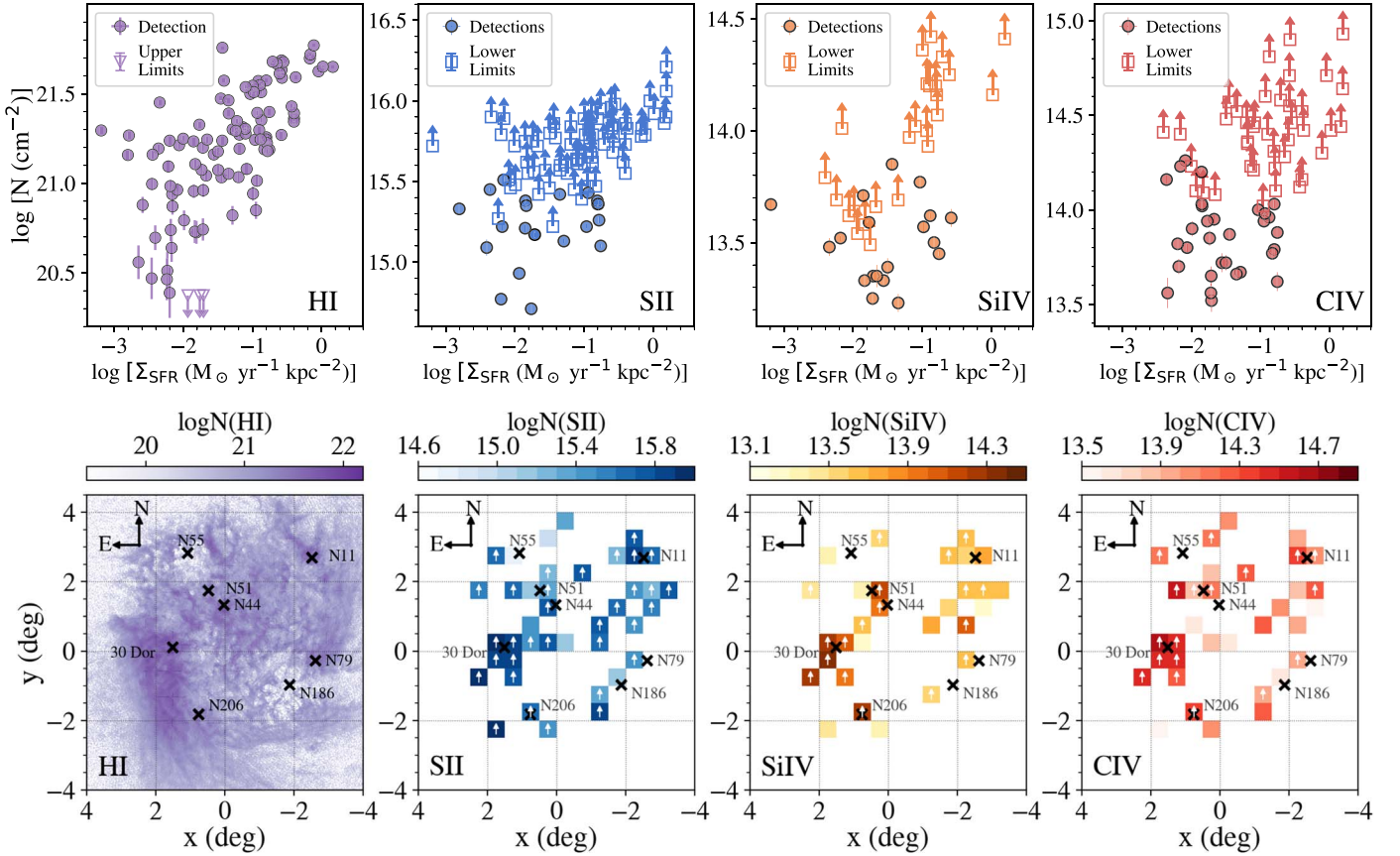
Figure 8. Top: gas column density as a function of Σ_{SFR} in logarithmic values for H I, S II, Si IV, and C IV, respectively. Solid circles are detections, open squares with upward arrows are saturations with lower limits (only in S II, Si IV, and C IV), and open triangles with downward arrows are nondetections (only in H I). The error bars on the x-axis ($\sim$0.02–0.06 dex) are smaller than the symbol sizes. Bottom: 2D spatial distributions of H I, S II, Si IV, and C IV column densities in the same orthographic projection as shown in Figure 3. For S II, Si IV, and C IV, the shown $\log N$ values/colors in bins noted with upward arrows should be considered as conservative lower limits. Several major H ii regions are highlighted as crosses in each panel. We find high ion column densities correlate with regions with high star-forming activities, such as 30 Dor at $x \sim 1°\!5$ and $y \sim 0°$. See Section 4.1 for further details.

corresponding spatial bin to indicate a lower limit. We have checked that the choice of mean or median values does not change the overall $\log N$ patterns shown in the 2D maps.

We find that regions with high ion column densities coincide with active star-forming sites, such as 30 Dor near $x \sim 1°\!5$ and $y \sim 0°$. The correlation between ion column densities and Σ_{SFR} suggests that star formation activities in the past $\sim$7–10 Myr, as traced by Hα emission, significantly impact the distribution of gas in all phases across the LMC.

4.2. Detection of Disk-wide Outflows in the LMC

In Figure 9, we show how the bulk velocities of the LMC's multiphase gas offset from its young stellar disk kinematics as a function of Σ_{SFR}. We define a velocity offset as

$$\delta v_{\mathrm{bulk, x}} \equiv v_{\mathrm{helio, x}} - v_{\mathrm{RSG}}, \qquad (5)$$

where $v_{\mathrm{helio, x}}$ is the centroid velocity of an ion with x being H I, S II, Si IV, or C IV, and v_{RSG} is the line-of-sight velocity of the LMC's stellar disk as represented by RSGs (see Section 3.3). The values of $v_{\mathrm{helio, x}}$ and v_{RSG} for the ULLYSES DR5 sight lines can be found in Table 2.

For H I, because the 21 cm emission comes from both the front side and backside of the LMC disk, the signs in $\delta v_{\mathrm{bulk, HI}}$ cannot be used to diagnose inflows or outflows. The top left panel shows that most of the neutral gas probed by H I has bulk velocities consistent with those of the RSGs within

$\sim$20 km s^{-1}. The similarity between H I kinematics and that of the RSGs suggests that the bulk mass of the H I gas in the LMC is corotating with the underlying young stellar disk (see also Olsen & Massey 2007; Olsen et al. 2011).

When considering the ionized gas, Figure 9 shows that the bulk velocities of S II, Si IV, and C IV are preferentially offset toward negative values. Given that the stellar sight lines only probe absorption by gas in the foreground of the stars, negative δv_{bulk} values in the ion panels indicate outflowing gas from the LMC toward our lines of sight. Hereafter, we refer to those data points with $\delta v_{\mathrm{bulk}} < -15$ km s^{-1} as outflows, and discuss the outflow velocities in absolute values as $|v_{\mathrm{out, bulk}}|$.

Figure 9 shows that the bulk velocities of the ionized outflows are over a range of $|v_{\mathrm{out, bulk}}| \sim 20$–60 km s^{-1}. Note that the $|v_{\mathrm{out, bulk}}|$ values are projected outflow velocities along our lines of sight, and they should be considered as lower limits to the actual outflow velocities in the LMC; in Section 5, we discuss the impact of the LMC's inclination and other factors on the observed outflow velocities.

We find S II, Si IV, and C IV outflows commonly detected over $\Sigma_{\mathrm{SFR}} \sim 10^{-2.5}$–$10^{-0.5}$ $M_\odot$ yr^{-1} kpc^{-2}, and the histogram distributions on the y-axes show that the Si IV and C IV outflows are moving faster than the S II outflows by $\sim$20–30 km s^{-1}. Toward the higher Σ_{SFR} end, outflows are only detected in Si IV and C IV but not in S II, which indicates that star-forming regions with high Σ_{SFR} are launching
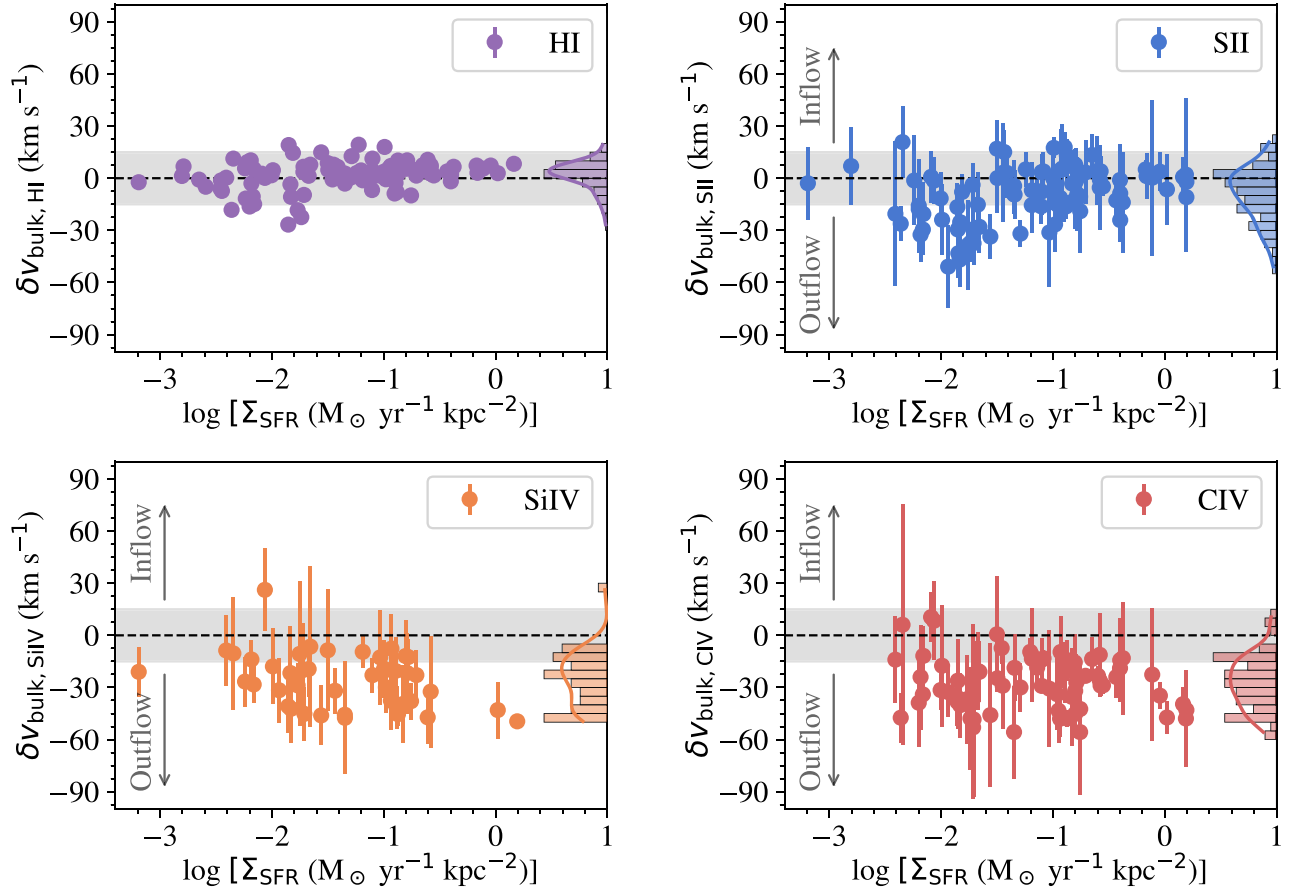
13

Figure 9. Velocity offsets between the multiphase gas (H I, S II, Si IV, and C IV) and the LMC's young stellar disk, $\delta v_{\rm bulk}$ (Equation (5)), as a function of $\Sigma_{\rm SFR}$. The bars on the right sides show histogram distributions of $\delta v_{\rm bulk}$. The top left panel shows that the H I gas largely follows the rotation of the LMC's young stellar disk. For S II, Si IV, and C IV, negative offset velocities indicate outflows; we refer to the negative values at $\delta v_{\rm bulk} < -15 \ {\rm km \ s}^{-1}$ as outflow velocities and discuss them in absolute values $|v_{\rm out, \ bulk}|$. We conservatively do not consider data points within $|\delta v_{\rm bulk}| < 15 \ {\rm km \ s}^{-1}$ (gray bands) to avoid the LMC's ISM. Generally, we find outflows in S II, Si IV, and C IV with bulk velocities of $|v_{\rm out, \ bulk}| \sim 20$–$60 \ {\rm km \ s}^{-1}$, suggesting that the bulk mass of the outflowing gas should be gravitationally bound. At the higher $\Sigma_{\rm SFR}$ end, we only detect outflows in Si IV and C IV but not in S II, suggesting that star-forming regions with higher $\Sigma_{\rm SFR}$ are likely to launch outflows that are more ionized. See Section 4.2 for further details.

outflows that are likely to be more ionized. We further investigate whether the outflows with high ionization states and in regions with high $\Sigma_{\rm SFR}$ are preferentially associated with Wolf–Rayet stars or O types earlier than O5, but do not find any significant correlation.

For Si IV, we find a significant correlation between the outflow velocities and $\Sigma_{\rm SFR}$ using Kendall's τ test with $p_{\rm Si \ IV} = 0.04$ (bottom left panel); however, for S II and C IV, we do not find any significant correlation. In general, Figure 9 shows large scatters in the outflow velocities with respect to $\Sigma_{\rm SFR}$. The scatters in the outflow velocities are likely to be caused by multiple factors, such as outflow opening angles, ages, and locations (i.e., outflows launched at different times may reach different heights and may not correlate well with present-day SFR traced by Hα). We further discuss the scatters in Section 5.

Lastly, in Figure 10, we show 2D spatial distributions of $\delta v_{\rm bulk}$ for S II, Si IV, and C IV. The $\delta v_{\rm bulk}$ values are averaged over $0°.5 \times 0°.5$ bins to bring out the large-scale kinematic pattern across the LMC. The color bars are arranged such that gray pixels represent regions with ionized gas velocities consistent with the LMC's stellar disk (and ISM) within $\pm 15 \ {\rm km \ s}^{-1}$, and blue pixels highlight regions with outflows. We find that the Si IV and C IV outflows are commonly found near major H II regions. Some H II regions with high $\Sigma_{\rm SFR}$,

such as 30 Dor, do not have outflows in S II, which is likely due to outflows being more ionized in these regions, as is also shown in Figure 9.

Simulations have shown that a majority of outflow mass is found to be in the cool-warm phase (e.g., Li et al. 2017; Kim et al. 2020; Rathjen et al. 2021), which is typically traced by the ions that are studied in this work. Given that the observed outflow velocities are within the escape velocity of the LMC near the disk ($v_{\rm esc} \sim 90 \ {\rm km \ s}^{-1}$) (Barger et al. 2016), the bulk mass of the outflowing gas should be gravitationally bound to the LMC. The outflowing gas is thus likely to be part of the LMC's galactic fountain flows and would eventually reverse its course and become inflows toward the LMC at cooler phases, as typically seen in outflow simulations (e.g., Kim & Ostriker 2018; Kim et al. 2020). However, in Figure 10, the ionized outflows are commonly detected across the LMC disk in all ions, while inflows are not as common. The rare exceptions are two bins in S II near $(x, y) \sim (2°, -1°.5)$, and one bin in Si IV near $(x, y) \sim (-2°, 2°)$. We discuss potential causes for these rare inflow detections in Section 6.5.

4.3. Outflows Corotating with the LMC Disk

In Figure 11, we show the 2D distributions of H I, S II, Si IV, and C IV bulk velocities in the heliocentric frame. The H I
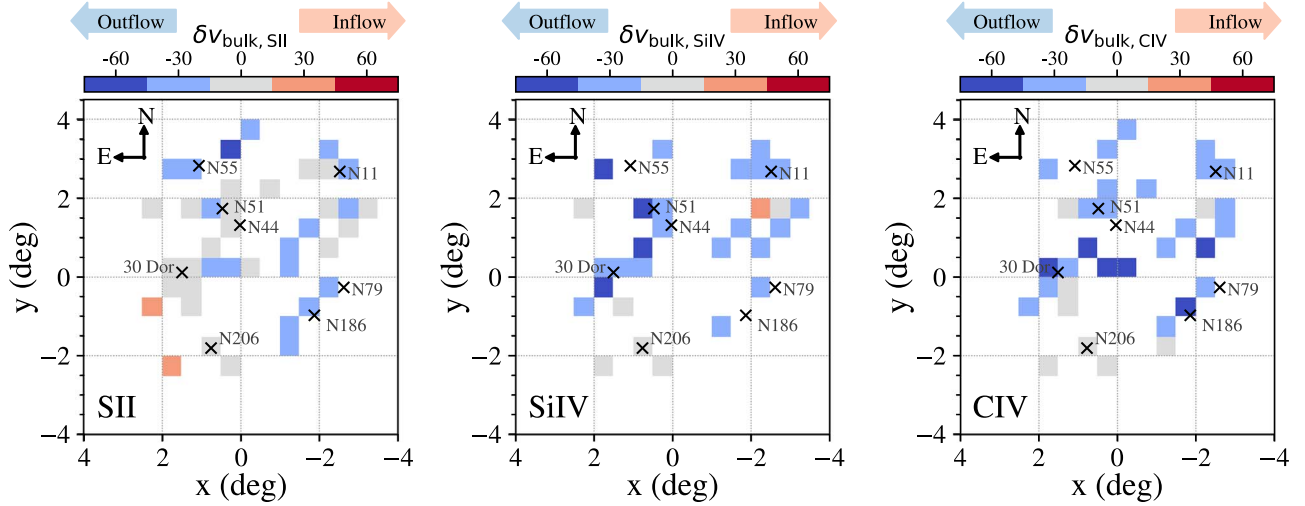
Figure 10. 2D distribution of $\delta v_{\rm bulk}$ (Equation (5)) for S II (left), Si IV (middle), and C IV (right) in the same orthographic projection as in Figure 3 and in units of kilometers per second. Gray indicates regions with ionized gas kinematics consistent with the LMC's stellar disk (and ISM) within ± 15 km s^{-1}, blue for bulk outflows, and red for bulk inflows. Major H II regions are indicated by crosses. We find disk-wide ionized outflows in S II, Si IV and C IV with bulk velocities of $|v_{\rm out,\,bulk}| \sim 20$–60 km s^{-1}. See Section 4.2 for further details.
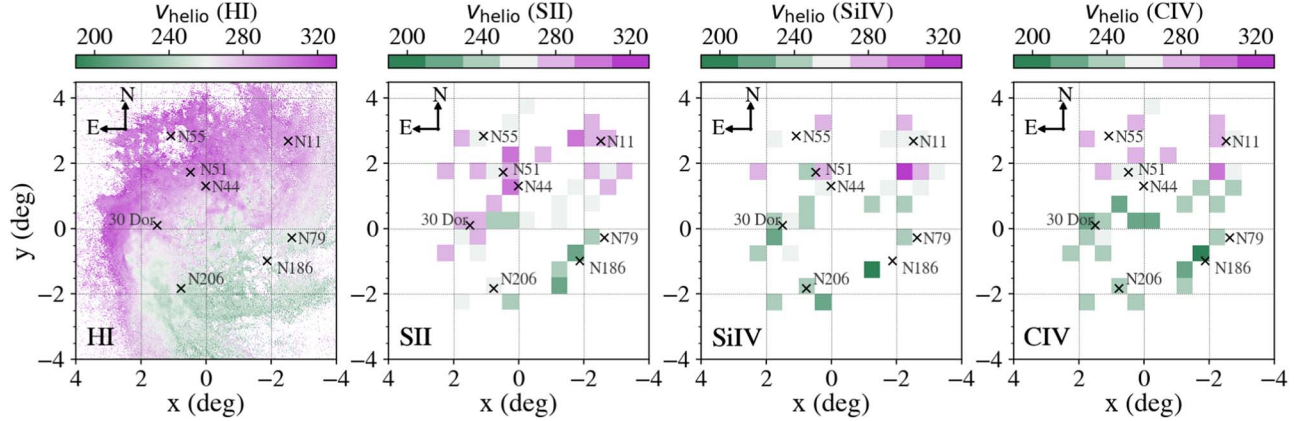
Figure 11. 2D distributions of H I, S II, Si IV, and C IV bulk velocities in the heliocentric frame and in units of kilometers per second. The systemic velocity of the LMC at the center of its mass $(x, y) = (0°, 0°)$ is $v_{\rm sys} = 264$ km s^{-1} (Choi et al. 2022), which is shown as a gray color. Major H II regions are indicated by black crosses. All ions show signs of corotation with the LMC's disk. See Section 4.3 for further details.

moment one map (left panel) is based on the 21 cm emission data cube from Kim et al. (2003) as discussed in Section 3.2, while the S II, Si IV, and C IV are measured along the ULLYSES sight lines and averaged over $0.°5 \times 0.°5$ bins in the same way as for the $\log N$ values discussed in Section 4.1.

The H I panel shows that the northeast half of the LMC disk is moving away from us at a faster speed of $v_{\rm helio} \sim 280$–320 km s^{-1}, while the southwest half is moving slower at $v_{\rm helio} \sim 200$–240 km s^{-1}. Note that the northeast half of the LMC disk is closer to us (van der Marel et al. 2002), and the LMC is rotating clockwise. In the S II, Si IV, and C IV panels, we find that the ions' bulk velocities exhibit a rotation pattern similar to the one in H I, indicating that the ionized outflows are corotating with the LMC disk.

In all, Figures 8–11 show a coherent picture that the LMC is currently launching disk-wide, warm-ionized outflows with bulk velocities of $|v_{\rm out,\,bulk}| \sim 20$–60 km s^{-1}. The bulk mass of the outflowing gas should be gravitationally bound to the LMC, and is corotating with the LMC. Star-forming regions with higher $\Sigma_{\rm SFR}$ are launching outflows that are likely to be more ionized.

5. A Scaling Relation between Outflow Velocities and Star Formation

We compare our LMC outflow measurements with both theoretical predictions and existing outflow observations in nearby star-bursting galaxies in Figure 12. For theoretical predictions, we focus on simulated data adopted from Kim et al. (2020), which study how multiphase outflows develop in a suite of parsec-resolution simulations over a wide range of star-forming conditions with $\Sigma_{\rm SFR} \sim 10^{-4.5}$–$1\,M_\odot\,{\rm yr}^{-1}$ using the TIGRESS-classic framework (Kim & Ostriker 2017, 2018). For existing outflow observations, we consider data from Heckman et al. (2015, hereafter H15), Chisholm et al. (2015, hereafter, C15), and Xu et al. (2022, hereafter, X22), which also examine ionized outflows with $T \sim 10^{4-5}$ K in commonly accessible ions such as Si II, Si III, Si IV, and C IV. Because these works measured outflows using either the same or similar instruments (either HST or FUSE spectroscopy[22]), the
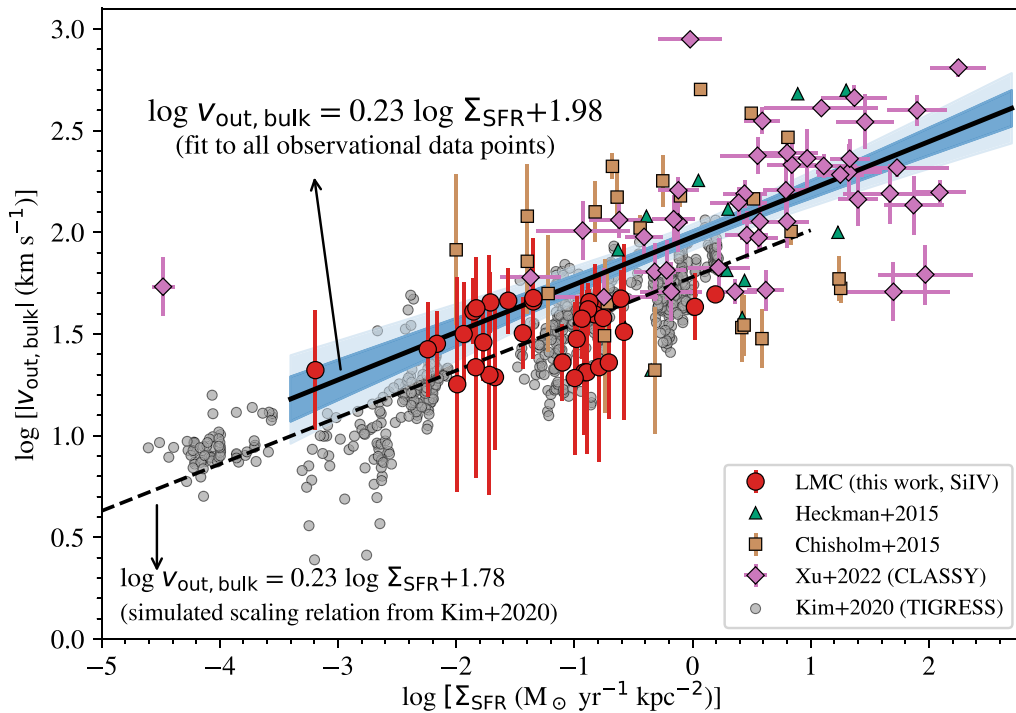

Figure 12. A scaling relation between bulk outflow velocity and Σ_{SFR} in logarithmic values. We compare the LMC outflows (red-filled circles) with three studies, including H15, (green-filled triangles), C15 (yellow-filled squares), and X22 (magenta-filled diamonds), on cool outflows in starburst galaxies that used the same or similar instruments (either HST or FUSE) to minimize systemic uncertainties. The solid black line shows our best-fit power-law relation, $\log v_{out, bulk} = 0.23 \log \Sigma_{SFR} + 1.98$ or $v_{out, bulk} = 95.5 \text{ km s}^{-1} \Sigma_{SFR}^{0.23}$, for the observational data points, where the dark and light blue shades indicate the 68% and 95% confidence intervals. Gray-filled circles show simulation predictions from the TIGRESS-classic simulation suite over a wide range of star-forming conditions (Kim et al. 2020). The best-fit scaling relation from Kim et al. (2020) is shown as a black dashed line. See Section 5 for further details.

comparison below avoids significant systemic uncertainties such as differences in spectral resolution and outflow phases. Note that the galaxy samples from these three studies are not mutually exclusive. We elaborate on the key aspects of each work, and adopt the most recent measurements for galaxies that have been used in more than one study.

H15 studied warm outflows in 39 starburst galaxies at $z < 0.2$ using Si III (COS) and N II and C III (FUSE), and their galaxy sample covers a parameter space of $M_* = 10^{7.1-10.9} M_\odot$ and SFR = 0.016–66 $M_\odot \text{ yr}^{-1}$. C15 examined outflows traced by Si II in 48 star-forming galaxies with $M_* = 10^{7.3-11.4} M_\odot$ and SFR = 0.02–136.8 $M_\odot \text{yr}^{-1}$ at $z = 0.0007–0.26$. Both studies measured bulk velocities of outflows (center of mass) using weighted average velocities, similar to what we did for the LMC outflows.

C15 noted that Si II may not be a perfect tracer of warm-ionized outflows because it only requires 8.2 eV to produce and 16.3 eV to ionize, which means the ion traces both neutral and ionized outflows. However, a follow-up study by Chisholm et al. (2016) using the same sample[23] showed that outflows probed by different ions such as O I, Si II, Si III, and Si IV are most likely to be comoving and cospatial given the similarity in the derived outflow velocities and widths. Therefore, in Figure 12, we compare the LMC's Si IV outflows with C15's Si II measurements without additional correction.

X22 studied galactic outflows in 45 starburst galaxies with $M_* \sim 10^{6-10} M_\odot$ and SFR $\sim$0.01–100 $M_\odot \text{ yr}^{-1}$ at $0.002 < z < 0.182$. For each galaxy, they fit Gaussian profiles to ISM

absorption, and when available, outflow absorption lines in O I, C II, Si II, Si III, and Si IV. The final outflow velocities are taken as the median values of outflows detected in all available ion lines along the corresponding sight lines. Because the contribution of the ISM absorption has been taken out, by design, their outflow velocities would be slightly faster than those measured for the same galaxies using simply weighted centroid velocities. Therefore, the outflow velocities adopted from X22 may be systematically higher than the rest because of their different method.

Figure 12 shows the outflow velocities as a function of Σ_{SFR}; the simulated predictions from Kim et al. (2020) are shown as gray-filled circles, while the observational data are shown as red-filled circles for the LMC, green-filled triangles for H15, yellow-filled squares for C15, and magenta-filled diamonds for X22. In a solid black line, we show our linear regression fit, $\log v_{out, bulk} = \beta \log \Sigma_{SFR} + \alpha + \sigma$, to the observational data points in log-log space using a Python version[24] of the `linmix` package detailed in Kelly (2007), where β is the slope, α the intercept, and σ the intrinsic scatter of the data points about the regression. The linear regression is performed over $\Sigma_{SFR} = 10^{-3.4}–10^{2.7} M_\odot \text{ yr}^{-1} \text{ kpc}^{-2}$, excluding the outlier at $\Sigma_{SFR} \sim 10^{-4.5} M_\odot \text{ yr}^{-1} \text{ kpc}^{-2}$ from X22. We find a best-fit scaling relation of

$$\log\left(\frac{v_{out, bulk}}{\text{km s}^{-1}}\right) = 0.23^{+0.03}_{-0.03} \log\left(\frac{\Sigma_{SFR}}{M_\odot \text{ yr}^{-1} \text{ kpc}^{-2}}\right)$$
$$+ 1.98^{+0.03}_{-0.03} \pm 0.29, \qquad (6)$$

---

[23] Chisholm et al. (2016) studied 37 star-forming galaxies, which is a subset of C15's because of an implementation of 3σ cut in equivalent widths to only select galaxies with significant outflow detections.

[24] https://github.com/jmeyers314/linmix

where the errors for the coefficients α and β are the 84th$-$50th and 16th$-$50th percentile differences from the posterior distributions. During the fitting, because H15's outflow velocities do not include errors, we assume a uniform error of $e_v = 28$ km s^{-1}, which is the median outflow velocity error from X22. Additionally, neither C15 nor H15 reported errors in their log Σ_{SFR} values; we assume a uniform error of 18% of the corresponding log Σ_{SFR} value, which is the typical median error of X22's log Σ_{SFR} measurements. We note that the linear regression result does not change significantly if we use the LMC's C IV outflow measurements instead of Si IV.

Given that the observational data points from H15, C15, and X22 dominate the middle to higher end of the $v_{out,\,bulk}$–Σ_{SFR} distribution in Figure 12, it is not surprising that our power-law index of 0.23 is consistent with what has been typically found in the literature ($v_{out,\,bulk} \propto \Sigma_{SFR}^{0.1-0.2}$) (Martin 2005; Rupke et al. 2005; Chen et al. 2010; C15; Rupke 2018; Reichardt Chu et al. 2024). What is remarkable is that, in spite of spanning 5 orders of magnitudes in Σ_{SFR}, there is a coherent scaling relation between the outflow velocities and star formation activities, with the LMC at the lower end.

Our fit also agrees remarkably well with what is predicted by Kim et al. (2020), which find a scaling relation of $\log v_{out,\,bulk} = 0.23 \log \Sigma_{SFR} + 1.78 \pm 0.14$ for cool outflows over a broad range of star-forming conditions at $\Sigma_{SFR} \sim 10^{-4.5}-1\,M_\odot$ yr^{-1} kpc^{-2} (black dashed line in Figure 12). The main discrepancies are the intercept and the intrinsic scatter. For the observations, we find an intercept of $\alpha = 1.98$ (or $v_{out,\,bulk} = 95.5$ km s^{-1}), while Kim et al. predict a lower intercept of $\alpha = 1.78$ (or $v_{out,\,bulk} = 60.3$ km s^{-1}). Meanwhile, the observations show an intrinsic scatter of $\sigma = 0.29$ dex, which is twice as high as the predicted intrinsic scatter ($\sigma = 0.14$ dex). Given that the LMC data points (red-filled circles) in Figure 12 generally match well with the simulation predictions (gray-filled circles) over the same Σ_{SFR}, we suspect that the discrepancies between our fit and Kim et al.'s are mainly driven by the observational data points at the higher Σ_{SFR} end from H15, C15, and X22.

There are likely to be several reasons for the discrepancies between observations and simulations. Physically, it is possible that star-bursting galaxies from H15, C15, and X22 are driving much faster outflows, which elevate our fit in Figure 12. Furthermore, each data point from H15, C15, and X22 represents a single galaxy or a large fraction of a star-forming disk within an instrument's aperture, which traces spatially averaged galactic scale outflows. These galaxies or regions of galaxies were generally selected for their UV brightness and may be biased toward regions where powerful outflows have already cleared some of the ISM. In contrast, both our LMC measurements and Kim et al.'s simulations focus on sub-kiloparsec scale localized outflows that are sensitive to temporal, weak outflow signals from individual star-forming regions. Lastly, different methods in calculating outflow velocities among the works may also contribute to the discrepancies.

As for the scatters, as discussed in C15, there are a number of factors that could cause the scatters such as galaxy inclinations, outflow driving mechanisms (energy or momentum driven), and CGM masses of host galaxies which would impact the propagation of outflows as they leave the disks. Different methods used to derive Σ_{SFR} may also contribute to the scatters. For example, H15 and C15 computed their SFR values based on UV and infrared fluxes of galaxies with

prescriptions from Kennicutt & Evans (2012), while X22's SFR values are based on broadband spectral energy distribution (SED) fittings by Berg et al. (2022). And H15 and X22 calculated their Σ_{SFR} values averaged within half-light radii of their sample galaxies, but C15's values are measured within the COS aperture.

The remarkable similarity, but also discrepancies, between observational and simulated outflows warrant further investigation, which is beyond the scope of this work. The key message from Figure 12 is that, dwarf galaxies like the LMC are capable of launching outflows not only in star-bursting regions such as 30 Dor, but also in regions with low star formation surface densities. And despite systemic differences in measurement methods, there is a universal scaling relation between outflow velocities and Σ_{SFR}, $v_{out,\,bulk} \propto \Sigma_{SFR}^{0.23}$, across a wide range of star-forming conditions at $\Sigma_{SFR} \sim 10^{-4.5}-10^2\,M_\odot$ yr^{-1} kpc^{-2}.

6. Discussion

6.1. Conservative Estimates on Outflow Mass, Outflow Rate, and Mass-loading Factor

We estimate the LMC's bulk outflow mass M_{out}, outflow rate $\dot{M}_{out}$, and mass-loading factor η ($\equiv \dot{M}_{out}/$SFR) by considering the outflows from both sides of the disk. We assume that the backside outflows, though not observable with ULLYSES, are similar to those in the nearside. The assumption is based on Barger et al. (2016)'s star-QSO pair observation that ion absorptions due to outflows from both sides of the LMC show similar absorption depths and velocity spans (see Section 6.3).

The following calculations are based on measurements of C IV. We choose C IV because there are more ULLYSES sight lines with reliable C IV measurements (71/109) than with Si IV (44/110), as is shown in Figure 3, which allows us to better estimate the outflow covering fraction across the LMC. Our estimates should be treated as conservative lower-limit values, given that most of the C IV outflows are saturated (see Figure 8) and we assume the maximum C IV ionization fraction of $f_{CIV} = 0.3$ possible through either equilibrium collisional ionization or photoionization (Gnat & Sternberg 2007).

We simplify the LMC outflows as gas moving in a cylindrical volume with a total mass of

$$M_{CIV} = 2 \times m_C \times (N_{CIV} \times \cos i) \times \pi R_{out}^2 \times c_f$$
$$\gtrsim 2.7 \times 10^2\,M_\odot \left(\frac{N_{CIV}}{10^{14}\,\text{cm}^{-2}}\right) \left(\frac{R_{out}}{3.5\,\text{kpc}}\right)^2 \left(\frac{c_f}{0.4}\right), \quad (7)$$

where the factor of 2 is to take into account the LMC's backside outflows and m_C is the mass of a carbon atom. We set $N_{CIV} \approx 10^{14}$ cm^{-2}, which is the characteristic column density where C IV begins to saturate (see Figure 8), and the factor of $\cos i$ is to correct for the increased path length through the outflowing layer due to the LMC's inclination $i = 23°4$ (see Table 1). $R_{out} \approx 3.5$ kpc is the maximum in-plane radius probed by our sight lines that show clear detections of outflows (see Figure 10).

We find a C IV outflow covering fraction of $c_f \approx 0.4$ (14/33) by counting the number of bins in Figures 8 and 10 with $\bar{N}_{CIV} \geqslant 10^{14}$ cm^{-2} and $\delta v_{bulk,\,CIV} \leqslant -15$ km s^{-1}, and then dividing the value by the number of bins with reliable C IV measurements. We choose to calculate c_f based on the spatially averaged 2D maps because it avoids oversampling outflows in high star-forming regions, such as 30 Dor, which are probed by

many ULLYSES sight lines simultaneously. Varying the bin sizes of $0°5 \times 0°5$ to smaller ($0°3 \times 0°3$) or larger ($1°0 \times 1°0$) grids only changes the c_f value by ~ 0.1.

We assume that the outflows have the same metallicity as the LMC's ISM ($Z_{out} \approx 0.5\,Z_\odot$) and estimate the total mass of the outflows to be

$$M_{out} = 1.4m_p \times \frac{M_{CIV}}{f_{CIV} \times m_C \times Z_{out} \times [C/H]_\odot}$$
$$\gtrsim 8 \times 10^5\,M_\odot \left(\frac{f_{CIV}}{0.3}\right)^{-1}\left(\frac{Z_{out}}{0.5\,Z_\odot}\right)^{-1}, \qquad (8)$$

where the factor of 1.4 is to account for the helium mass, and $[C/H]_\odot = 10^{8.43-12.0}$ is the solar photosphere abundance (Asplund et al. 2009).

Recent analyses of the LMC's star formation history show that the galaxy is currently experiencing a high star-forming episode that began ~ 30 Myr ago (Mazzi et al. 2021). We assume that the LMC began to launch the most recent outflows around the same time and has continued driving outflows until the present day with a time duration of $t_{out} \sim 30$ Myr. The LMC's mass outflow rate and the mass-loading factor are

$$\dot{M}_{out} = M_{out}/t_{out} \gtrsim 0.03\,M_\odot\ \mathrm{yr}^{-1}\left(\frac{t_{out}}{30\,\mathrm{Myr}}\right)^{-1}$$
$$\eta = \dot{M}_{out}/\mathrm{SFR} \gtrsim 0.15, \qquad (9)$$

where SFR $\approx 0.2\,M_\odot\,\mathrm{yr}^{-1}$ is the global SFR of the present-day LMC adopted from Harris & Zaritsky (2009) and Mazzi et al. (2021).

When compared with literature values, we find that our M_{out} and $\dot{M}_{out}$ values are consistent with Barger et al. (2016)'s estimates for the LMC based on their C IV measurements (see their Table 4). Note that our estimates should be treated as strictly conservative values, given that the C IV outflows are mostly saturated in the LMC and we assume the maximum ionization fraction.

Our mass-loading factor of $\eta \gtrsim 0.15$ is a factor of ~ 10 lower than those measured by Chisholm et al. (2017) for galaxies at similar masses as the LMC, which have $\eta \sim 0.9$–2; the discrepancy here is likely due to the more active star-forming nature of Chisholm et al.'s galaxies with SFR ~ 3.6–$26\,M_\odot\,\mathrm{yr}^{-1}$, which may drive more powerful and efficient outflows. When considering galaxies with similar Σ_{SFR}, we find that our η value is within what is predicted by Kim et al. (2020)'s outflow simulations over $\Sigma_{SFR} \sim 10^{-3}$–$10^{-1}\,M_\odot\,\mathrm{yr}^{-1}\,\mathrm{kpc}^{-2}$, but about ~ 1–1.5 dex lower than their median values (see their Figure 8).

Lastly, considering the time duration of $t_{out} \sim 30$ Myr and a mean bulk outflow velocity of $\sim 30\,\mathrm{km\,s}^{-1}$ in C IV, we can infer that the bulk mass of the LMC outflows is at a height of $z_{out} \sim 0.9$ kpc. When compared to the LMC's disk scale height (~ 0.97 kpc from Cepheid stars; Ripepi et al. 2022), we find that the bulk outflow mass has not made it out of the LMC's disk. This is consistent with our observation in Figure 11 that the outflowing gas is still under the gravitational influence of the LMC's disk and thus shows kinematic signs of corotation with the disk.

6.2. Shielding of the LMC Outflows by a Potential Bow Shock

At a Galactocentric velocity of $321\,\mathrm{km\,s}^{-1}$ (Kallivayalil et al. 2013), the LMC is moving in the MW's halo with a Mach number of ~ 2.1 (Setton et al. 2023). Using an LMC-specific hydrodynamic simulation, Setton et al. (2023) showed that the LMC's supersonic movement is likely to generate a bow shock leading the LMC due to ram pressure from the MW, as is illustrated in Figure 1. The ram pressure impact has been well observed in the LMC's truncated H I disk (Salem et al. 2015), and it is likely that the ram pressure also shapes the morphology of the LMC's Hα emission (Smart et al. 2023; Setton et al. 2023). Although the existence of an LMC bow shock remains to be observationally tested, below we provide indirect evidence of this bow shock by speculating that it may have shielded the LMC outflows from the MW's ram pressure.

When a satellite galaxy orbits a massive host, its ISM gas is subject to ram pressure stripping from the halo of the massive host. This is commonly seen in dwarf galaxies closer to the MW and M31 (Putman et al. 2021), as well as in jellyfish galaxies in large galaxy groups and clusters (e.g., Poggianti et al. 2016). Zhu et al. (2023) showed that when a galaxy's disk is at an angle of $45°$ against the headwinds due to ram pressure, the gas above the galaxy disk is being swept downstream and flowing mainly parallel to the galaxy disk (see their Figure 13). Had the LMC experienced such strong ram pressure stripping, we would expect the outflowing gas to have been swept in the opposite direction of the LMC's proper motion (east to west), and the outflow column densities are unlikely to correlate with Σ_{SFR}.

Our analyses in Figures 8–11 show that the LMC outflows are well correlated with Σ_{SFR} in ion column densities, and the outflows are corotating with the LMC disk. Calculations in Section 6.1 suggest that the bulk mass of the outflowing gas is close to the LMC disk at a height of ≈ 0.9 kpc, which is well within the size of the bow shock predicted in Setton et al. (2023)'s LMC simulation. Additionally, Barger et al. (2016) showed that the LMC outflows in the nearside and backside show similar absorption strengths and velocity spans, indicating that the outflows on the nearside are not significantly suppressed. As there is no significant sign of the outflowing gas being impacted by external forces, such as ram pressure from the MW halo gas, we suspect that the LMC's outflows may have been shielded by a potential bow shock as the LMC orbits the MW supersonically.

6.3. Comparison with Previous LMC Gas Studies

In this section, we briefly compare our work with previous studies on the LMC gas over $v_{helio} \sim 175$–$375\,\mathrm{km\,s}^{-1}$. The key message is that the outflows we find are correlated with the most recent star formation episode of the LMC, and they are gravitationally bound to the LMC with $|v_{out,\,bulk}| \sim 20$–$60\,\mathrm{km\,s}^{-1}$, consistent with previous studies using smaller samples of stellar sight lines. These outflows are not connected to the high-velocity cloud at $v_{helio} \sim 90$–$175\,\mathrm{km\,s}^{-1}$ in the foreground of the LMC (see Figure 1); we discuss the physical properties of the high-velocity cloud and relevant studies in Section 6.4.

The LMC gas at $v_{helio} \sim 175$–$375\,\mathrm{km\,s}^{-1}$ is found to be multiphase as seen in both emission and absorption. Figure 2 shows that H I 21 cm is found across the galaxy tracing large- and small-scale neutral gas structures such as outer arms and supergiant shells (Kim et al. 2003; Staveley-Smith et al. 2003; Nidever et al. 2008). This neutral gas mainly follows the rotation of the LMC stellar disk, and does not show signs of outflows (see the top left panel of Figure 9). Smart et al. (2023) found that the Hα emission from the LMC is more extended

than the H I by several degrees, and the Hα gas kinematics is found to weakly trace the H I gas rotation.

Howk et al. (2002) studied O VI obtained from FUSE toward 12 LMC stellar sight lines over $175 \lesssim v_{LSR} \lesssim 375$ km s^{-1} (see also Danforth et al. 2002). The O VI column densities show a large variation, which is not correlated with underlying structures such as H I superbubbles. They found the O VI centroid velocities to be blueshifted from the LMC's low ion absorption lines (e.g., Fe II) by ~ -30 km s^{-1}, suggesting the presence of highly ionized outflows among these sight lines, consistent with our findings of outflows in Si IV and C IV.

Barger et al. (2016) probed a relatively quiet northwest region of the LMC using a pair of QSO-star sight lines in close projection over $165 \lesssim v_{LSR} \lesssim 415$ km s^{-1}. Ion spectra from both the star and the QSO show blueshifted outflows over ~ 165–280 km s^{-1}, while only the QSO spectra show redshifted outflows at ~ 280–415 km s^{-1} on the backside of the LMC disk. They found that the outflows in the nearside and backside show similar absorption strengths and velocity spans in O I, Si II, Al II, Si III, Si IV, and C IV.

Note that the ~ 100 km s^{-1} outflow speeds quoted by Barger et al. (2016) were measured toward the edge of the ion absorption, which represents the terminal velocities of the low-density outflowing gas. In contrast, the outflow velocities measured in this work as well as in Howk et al. (2002) are weighted outflow velocities representing the bulk mass of the outflowing gas. As shown in Figure 5, we also find outflows with high terminal velocities of $v \sim 100$ km s^{-1} toward the ULLYSES sight lines. However, we do not use the terminal outflow velocities in this work to avoid potential contamination due to the high-velocity cloud in the foreground, which we discuss in the next section.

6.4. The Foreground High-velocity Cloud at $v \sim 90$–175 km s^{-1}

A number of studies have noted the presence of a high-velocity cloud moving at $v_{helio} \sim 90$–175 km s^{-1} in the foreground of the LMC; hereafter, we refer to this cloud as HVC90-175. As sketched in Figure 1, Richter et al. (2015) constrained the distance to HVC90-175 to be within 13.3 kpc from the Sun using an HST/COS spectrum of a hot white dwarf (RX J0439.86809; Werner & Rauch 2015), which means HVC90-175 is located in the inner halo of the MW and at $\delta d \sim 40$ kpc from the LMC.

We show in Section 2.4 and Figure 5 that HVC90-175's absorption can be well constrained to be within $v_{helio} \lesssim 175$ km s^{-1} and the blending with the LMC absorption is relatively mild. Specifically, for Si IV (C IV) absorption, we find only 10/44 (22/71) sight lines with non-negligible blending between HVC90-175 and the LMC outflows near $v_{helio} = 175$ km s^{-1}. In these cases, the LMC is likely to launch fast outflows with terminal velocities of $\gtrsim 100$ km s^{-1} that are blended with HVC90-175. By focusing on the LMC absorption over $v_{helio} = 175$–375 km s^{-1} in this work, we minimize contamination from HVC90-175.

The origin of HVC90-175 remains debated. In Appendix A, we show that HVC90-175 is kinematically consistent with being an MW halo cloud at a constant velocity of $v_{LSR} \sim 120$ km s^{-1} (see also Savage & de Boer 1981; de Boer et al. 1990; Richter et al. 1999). The spread in line-of-sight velocities toward HVC90-175 can be well accounted for if we assume a temperature of $T \sim 10^{4.2}$ K and a nonthermal broadening of $\sigma_{nth} \sim 10$ km s^{-1} (see the details in Appendix A), which is

typical for MW halo clouds (Putman et al. 2012). The distance of HVC90-175, $d_\odot < 13.3$ kpc, is also consistent with other MW halo clouds (Wakker 2001).

We note that HVC90-175 has also been suggested to be associated with the LMC as a fast-moving, ancient outflow that was launched by the LMC's previous star-forming episode about $t_{SFR} \sim 250$–400 Myr ago (e.g., Barger et al. 2016; Ciampa et al. 2021). At a distance of $\delta d \sim 40$ kpc from the LMC, it would be challenging to launch an outflow that did not decelerate, increase the opening angle, or change trajectory. As the LMC moves through the MW halo in a nearly transverse direction (see the discussion in Section 6.2), the presumed ancient outflow would have been severely impacted by ram pressure when traveling such a large distance. Therefore, we consider it highly unlikely for HVC90-175 to originate from the LMC as an ancient outflow.

6.5. Rare Detection of Inflows

We note the rare detection of an inflow in Si IV toward a sight line, SK-67D22, at a velocity of $+26$ km s^{-1} with respect to the LMC's stellar disk, as is shown in the lower left panel of Figure 9. The corresponding C IV line shows a similar absorption profile, although its centroid velocity is $+8$ km s^{-1} because of the weighting algorithm that we apply in Section 2.4. SK-67D22 is located at $x \sim -2°$ and $y \sim 2°$ in Figure 10, which is the only bin in the Si IV panel that shows inflow detection. We examine SK-67D22's line spectra (not shown here), and find that the neutral (H I) and low ionization (S II) gas is moving at $v_{helio} \sim 290$ km s^{-1}, consistent with the underlying stellar disk ($v_{RSG} \sim 285$ km s^{-1}). The more ionized Si IV and C IV gas is found over $v_{helio} \sim 300$–340 km s^{-1}, indicating that the ionized gas is inflowing toward the LMC disk at $v_{in} \sim 10$–50 km s^{-1} in a relatively quiet region of the galaxy.

Similarly, there are two sight lines with S II inflows at $v_{in} \sim 15$–20 km s^{-1} in the southeast corner of the LMC where the star formation is less active (see Figures 3 and 10). In the heliocentric frame, the S II inflows are found at $v_{helio} \sim 300$ km s^{-1}, which coincides with the H I arm E of the LMC as identified by Staveley-Smith et al. (2003); we further investigate the connection between our S II detection and the arm E in a follow-up paper.

Overall, the detections of inflows in Si IV and S II suggest that the inflows may still exist in the LMC; they might be much weaker than the outflows along the same sight lines (see Figure 5), which would be averaged out in our calculation of optical depth weighted centroid velocities. Additionally, inflows might occur in areas that are relatively less sampled by the ULLYSES sight lines. Another possible explanation for the dominant outflow detection is that the LMC is currently undergoing an active star formation episode (Harris & Zaritsky 2009; Mazzi et al. 2021), which drives disk-wide outflows. Inflows may not occur until ~ 50–60 Myr later when outflows turn around, cool down, and rain back down to the disk, as seen in hydrodynamic simulations (e.g., Kim & Ostriker 2018). We further investigate the occurrence and physical properties of inflows in the LMC in a follow-up paper.

7. Summary

Using 110 stellar sight lines from the ULLYSES DR5 (Roman-Duval et al. 2020), we detect prevalent slow-moving,

ionized outflows ($|v_{\text{out, bulk}}| \sim 20\text{--}60 \,\text{km s}^{-1}$) in S II, Si IV and C IV across the disk of the LMC. Our work provides a direct comparison between spatially resolved outflows in a local galaxy (LMC) with aperture-averaged galactic outflows in star-bursting galaxies and simulation predictions. We demonstrate that there exists a universal scaling relation between outflow velocities and SFR surface densities, $|v_{\text{out, bulk}}| \propto \Sigma_{\text{SFR}}^{0.23}$, over a wide range of star-forming conditions with $\Sigma_{\text{SFR}} \sim 10^{-4.5}\text{--}10^2 \, M_\odot \, \text{yr}^{-1} \, \text{kpc}^{-2}$. We summarize the main analyses and findings as follows.

We study the LMC neutral and ionized gas over $v_{\text{helio}} = 175\text{--}375 \,\text{km s}^{-1}$ in H I, S II, Si IV, and C IV. The velocity range is chosen to encompass the LMC gas in all directions while avoiding contamination from a foreground high-velocity cloud at $d_\odot < 13.3 \,\text{kpc}$ (Figure 1). The ion lines are chosen for their relatively less saturated line profiles over the LMC's velocity range. We develop a continuum-fitting algorithm based on the concept of Gaussian process regression, and select reliable ion spectra with minimal contamination from stellar absorption. Our algorithm results in 91/110 reliable LMC measurements in S II, 44/110 in Si IV, and 71/109 in C IV (see Section 2 and Figures 3–7).

We find that the column densities of the LMC's neutral (H I) and ionized (S II, Si IV, C IV) gas increase with the star formation rate surface density Σ_{SFR}. Most of the Si IV and C IV measurements are heavily saturated with $N(\text{Si IV}) \gtrsim 10^{13.6} \,\text{cm}^{-2}$ and $N(\text{C IV}) \gtrsim 10^{14.0} \,\text{cm}^{-2}$, and all ions are saturated at $\Sigma_{\text{SFR}} \gtrsim 10^{-0.5} \, M_\odot \, \text{yr}^{-1} \, \text{kpc}^{-2}$. As Σ_{SFR} is derived based on Hα emission that traces the LMC's recent star formation in the past $\sim$7–10 Myr, the correlation between gas column densities and Σ_{SFR} suggests that the LMC's star-forming activities may have an impact on its multiphase gas over a short timescale (see Section 4.1 and Figure 8).

We compare the centroid velocities of the neutral (H I) and ionized (S II, Si IV, C IV) gas to the LMC's stellar kinematics in Section 4.2 and Figure 9, where the centroid velocities indicate the bulk motion of gas where most of the mass is. We find that the velocities of the ionized gas are systemically blueshifted from the LMC's stellar disk, which indicates prevalent outflows at bulk velocities of $|v_{\text{out, bulk}}| \sim 20\text{--}60 \,\text{km s}^{-1}$. While Si IV and C IV outflows are detected ubiquitously in the LMC, S II outflows are only found in regions with relatively low Σ_{SFR} ($\lesssim 10^{-0.5} \, M_\odot \, \text{yr}^{-1} \, \text{kpc}^{-2}$). This indicates that star-forming regions with high Σ_{SFR} are launching outflows that are likely to be more ionized.

We release the first 2D UV ion maps of the LMC in Figures 8–11, and show that the Si IV and C IV outflows are stronger (in column density) in high star-forming regions such as 30 Dor. Additionally, the Si IV and C IV outflows show signs of corotation with the LMC disk. Given that there is no significant sign of impact from external forces such as ram pressure from the MW, we suspect that the outflows are likely to be shielded behind a potential bow shock that is leading the LMC as the galaxy orbits the MW supersonically. The existence and exact location of this potential bow shock remains to be tested observationally (see Sections 4.3 and 6.2).

We estimate the physical properties of bulk outflows from both sides of the LMC using the C IV measurements, and find strictly conservative lower limits with a total outflow mass of $M_{\text{out}} \gtrsim 8 \times 10^5 \, M_\odot$, an outflow rate of $\dot{M}_{\text{out}} \gtrsim 0.03 \, M_\odot \, \text{yr}^{-1}$, and a mass-loading factor of $\eta \gtrsim 0.15$. When comparing with outflows detected in starburst galaxies from previous observations (H15; C15; X22), we find a universal scaling relation of

$|v_{\text{out, bulk}}| \propto \Sigma_{\text{SFR}}^{0.23}$ (Figure 12). Our measurements also agree remarkably well with what is predicted for cool outflows in the TIGRESS-classic simulation suite (Kim et al. 2020; see Section 5).

Lastly, we find an intrinsic scatter of 0.29 dex in the $v_{\text{out,bulk}} - \Sigma_{\text{SFR}}$ power-law relation for all observational data points combined (Equation (6)), which is a factor of $\sim$2 higher than the simulation prediction. As we discuss in Section 5, many factors may contribute to the intrinsic scatter, such as different methods in calculating $v_{\text{out,bulk}}$ and Σ_{SFR}, potential biases in selecting outflow-dominated galaxies, and intrinsic galaxy properties that have not been accounted for such as inclinations, outflow driving mechanisms, as well as host galaxies' CGM masses. We will continue investigating the LMC outflows (as well as inflows) in comparison with other observational and simulation measurements in follow-up studies.

Data Availability

We release our data products, including normalized S II, Si IV, and C IV lines and their corresponding best-fit continuum models (when available), as a High Level Science Product called "LMC-FLOWS" at MAST via doi:10.17909/hz0m-np43. The ULLYSES DR5 data set (Roman-Duval et al. 2020; Roman-Duval et al. 2020) can be found at doi:10.17909/t9-jzeh-xy14.

Facilities: HST (COS, STIS).

Software: Astropy (Astropy Collaboration et al. 2013, 2018, 2022), NumPy (Harris et al. 2020), George (Ambikasaran et al. 2015), Matplotlib (Hunter 2007).

Appendix
The Foreground High-velocity Cloud at $v \sim 90$–175 km s^{-1}

Section 6.4 shows that HVC90-175's absorption can be constrained to be at $v_{\rm helio} \lesssim 175$ km s^{-1} and it is located at $d_\odot < 13.3$ kpc (Richter et al. 2015; Werner & Rauch 2015). The cloud is observed in H I (de Boer et al. 1990; Staveley-Smith et al. 2003), Hα emission (Ciampa et al. 2021), molecular hydrogen (Richter et al. 1999; Tchernyshyov 2022), and UV absorption tracing ionized gas (e.g., Savage & de Boer 1981; Lehner & Howk 2007; Lehner et al. 2009; Barger et al. 2016; Roman-Duval et al. 2019). Here, we further discuss HVC90-175 based on UV measurements from the literature and newly obtained in this work. We show that the kinematics of HVC90-175 is consistent with being an MW halo cloud at $v_{\rm LSR} \sim 120$ km s^{-1} with a temperature of $T \sim 10^{4.2}$ K and a nonthermal broadening of $\sigma_{\rm nth} \sim 10$ km s^{-1}. As noted in Section 1, in the general direction of the LMC, the $v_{\rm helio}$ and $v_{\rm LSR}$ velocities are offset by $v_{\rm helio} - v_{\rm LSR} \sim 10$ km s^{-1}.

In Figure A1, we show HVC90-175's velocity distributions in O I, S II, Si IV, and C IV as a function of R.A.. The S II, Si IV, and C IV are weighted centroid velocities integrated over a velocity range of $v_{\rm helio} = 90$–175 km s^{-1} using the same ULLYSES sight lines as discussed in Section 2.4; here, we prioritize using the stronger lines of S II 1253, Si IV 1393, and C IV 1548 unless the absorption is saturated. The O I data points are adopted from Lehner et al. (2009), who studied HVC90-175 toward 139 FUSE sight lines in the direction of the LMC.

The ion velocities are shown in three reference frames: the LSR (left panel), the Galactic standard of rest (GSR; middle panel), and the LMC standard of rest (LMCSR; right panel). The velocity conversions among these frames are based on the equations given by Lehner et al. (2009) in their Section 3.2:

$$v_{\rm LMCSR} = v_{\rm GSR} + 86\cos\ell\cos b + 268\sin\ell\cos b - 252\sin b$$
$$v_{\rm GSR} = v_{\rm LSR} + 220\sin\ell\cos b.$$
$$(A1)$$

We note that the O I distribution in the right panel (VLMCSR) reproduces Lehner et al.'s Figure 5, in which they first noted that HVC90-175 shows an apparent velocity gradient with R.A. in the LMCSR frame (see also Roman-Duval et al. 2019).

When we examine the velocity distributions with R.A. in all three reference frames, we find that HVC90-175's velocity gradient can only be mildly observed in the LSR (left panel) and the GSR frames (middle panel). In Figure A2, we show the 2D $v_{\rm LSR}$ distribution of the HVC90-175's gas across the surface of the LMC in the same orthographic projection as in Figure 11. For S II and C IV, there is no apparent trend in $v_{\rm LSR}$; and in O I, the southwest half (bottom right corner in the left panel) is moving faster, which is in the opposite direction of the LMC's rotation.

To better understand HVC90-175's ion velocities, we model a hypothetical MW halo cloud lying in front of the LMC at a constant velocity of $v_{\rm LSR} = 120$ km s^{-1} and show the modeled velocity distributions as gray contours in Figure A1. The velocities of the modeled halo cloud are calculated for the same ULLYSES sight lines used in this work, and the contours are generated using the kdeplot function from the seaborn package.

The spreads in the velocities are calculated by assuming a temperature of $T = 10^{4.2}$ K for our S II measurements and a nonthermal broadening of $\sigma_{\rm nth} = 10$ km s^{-1}, which corresponds to a total velocity dispersion of $\sigma_v \equiv \sqrt{(k_{\rm B}T/m_{\rm S}) + \sigma_{\rm nth}^2} = 10.2$ km s^{-1}. The choice of $\sigma_{\rm nth} = 10$ km s^{-1} is based on what is typically measured for nonthermal broadening in the ionized CGM gas (Chen et al. 2023). We note that the match between the modeled and the observed data in Figure A1 would be further improved if we assumed a higher temperature ($T \gtrsim 10^{4.2}$ K), adopted measurements from the lighter ions such as O I, Si IV or C IV, or more contribution from nonthermal broadening.

The right panel of Figure A1 shows that the modeled halo cloud, which has a constant $v_{\rm LSR} = 120$ km s^{-1}, exhibits a similar velocity gradient with R.A. as the observed ion data. We thus demonstrate that the velocity gradient with R.A. in HVC90-175 is mainly caused by velocity transformation between rest frames. The kinematic signature of HVC90-175 is consistent with that of a foreground cloud moving at $v_{\rm LSR} \sim 120$ km s^{-1} with $T \sim 10^{4.2}$ K and a nonthermal broadening of $\sigma_{\rm nth} \sim 10$ km s^{-1}, which are physical properties commonly found in known high-velocity clouds in the MW and ionized CGM gas in low-redshift galaxies (Wakker 2001; Putman et al. 2012; Chen et al. 2023).

Additionally, previous studies have measured the metallicity of HVC90-175 to be at [O I/H I] $= -0.51^{+0.12}_{-0.16}$ dex (Lehner et al. 2009) and an ion ratio of $N_{\rm OVI}/N_{\rm CIV} \sim 1$–10 (Lehner & Howk 2007). HVC90-175's metallicity is consistent with those of high-velocity clouds in the MW such as Complex C ($Z \sim 0.1$–$0.3\,Z_\odot$) (Shull et al. 2011), and its ion ratio is also consistent with those measured in the MW's ionized gas in various directions ($N_{\rm OVI}/N_{\rm CIV} \sim 1$–7) (Sembach et al. 2003, see their Table 11).

Lastly, we note that there is a small sample of O I absorbers at R.A. ~ 5 hr or $\sim 75^\circ$ that cannot be accounted for by our MW halo cloud model in Figure A1. The O I gas at this R.A. is moving at $v_{\rm LSR} \sim 150$–175 km s^{-1} and located at the west half of the LMC disk, which are shown as pink-purple pixels in Figure A2. Coincidentally, the LMC's neutral and ionized gas in this area is also moving at a similar velocity of $v_{\rm LSR} \sim 200$ km s^{-1}, as shown in Figure 11. It is possible that the excess O I absorbers with $v_{\rm LSR} \sim 150$–175 km s^{-1} near R.A. ~ 5 hr are either an extension of the LMC's gas with low $v_{\rm LSR}$ or blended with the LMC at similar velocities.
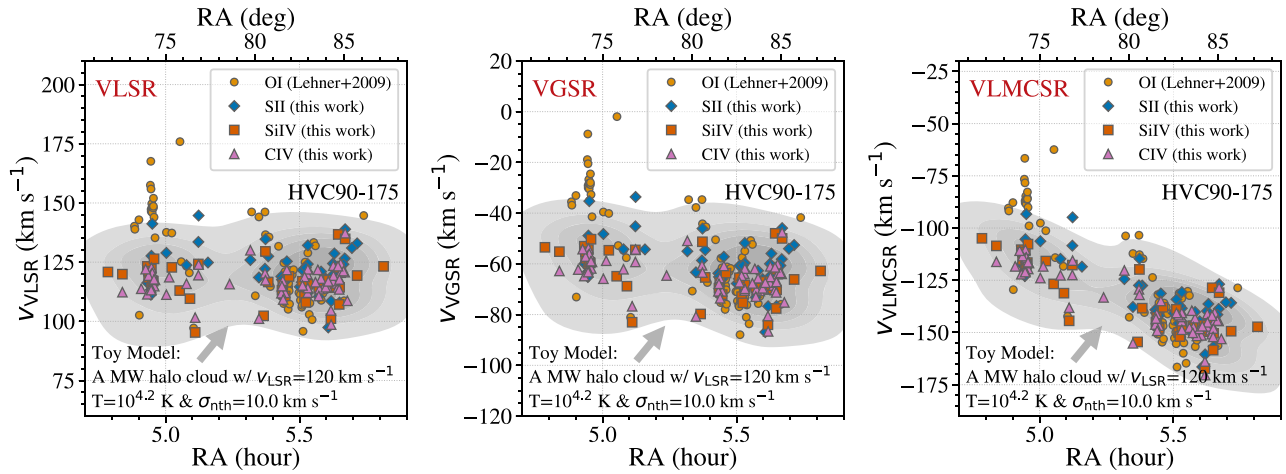
Figure A1. Multiphase ion velocities of HVC90-175 as a function of R.A. in the LSR (left), GSR (middle), and LMCSR (right) frames (see Equation (A1)). HVC90-175 is detected in low ions such as O I (yellow-filled circles; Lehner et al. 2009, see also Roman-Duval et al. 2019) as well as in S II, Si IV, and C IV (this work). HVC90-175's gas kinematics is consistent with being an MW halo cloud at $v_{LSR} = 120$ km s^{-1} with a temperature of $T = 10^{4.2}$ K and a nonthermal broadening of $\sigma_{nth} \sim 10$ km s^{-1}. The distance to HVC90-175 is constrained to be $d_\odot < 13.3$ kpc (Richter et al. 2015; Werner & Rauch 2015).
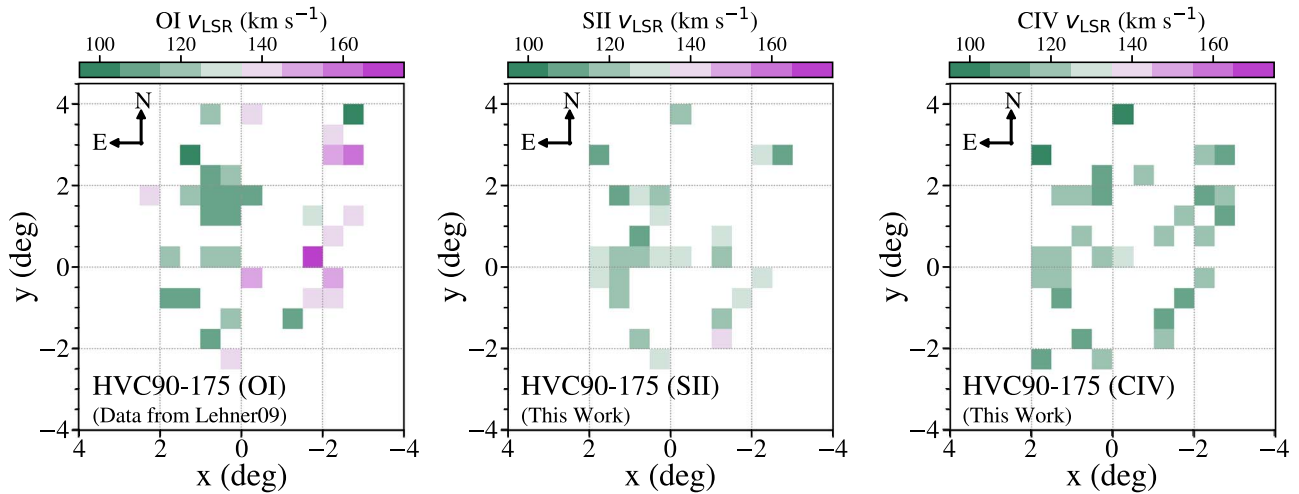
Figure A2. 2D velocity distributions of HVC90-175 in the same orthographic projection as in Figure 11. In the left panel, we find that the O I gas, as measured by Lehner et al. (2009), is moving faster at $v_{LSR} \sim 150$–175 km s^{-1} toward the west. Meanwhile, S II (middle), Si IV (not shown), and C IV (right) show nearly constant v_{LSR} at $\sim$120 km s^{-1} across the surface of the cloud.

ORCID iDs

Yong Zheng (郑永) ⓘ https://orcid.org/0000-0003-4158-5116
Kirill Tchernyshyov ⓘ https://orcid.org/0000-0003-0789-9939
Knut Olsen ⓘ https://orcid.org/0000-0002-7134-8296
Yumi Choi ⓘ https://orcid.org/0000-0003-1680-1884
Chad Bustard ⓘ https://orcid.org/0000-0002-8366-2143
Julia Roman-Duval ⓘ https://orcid.org/0000-0001-6326-7069
Enrico M. Di Teodoro ⓘ https://orcid.org/0000-0003-4019-0673
Jessica Werk ⓘ https://orcid.org/0000-0002-0355-0134
Mary Putman ⓘ https://orcid.org/0000-0002-1129-1873
Anna F. McLeod ⓘ https://orcid.org/0000-0002-5456-523X
Yakov Faerman ⓘ https://orcid.org/0000-0003-3520-6503
Raymond C. Simons ⓘ https://orcid.org/0000-0002-6386-7299
Joshua Peek ⓘ https://orcid.org/0000-0003-4797-7030

References

Ambikasaran, S., Foreman-Mackey, D., Greengard, L., Hogg, D. W., & O'Neil, M. 2015, ITPAM, 38, 252

Ambrocio-Cruz, P., Le Coarer, E., Rosado, M., et al. 2016, MNRAS, 457, 2048
Andersson, E. P., Agertz, O., Renaud, F., & Teyssier, R. 2023, MNRAS, 521, 2196
Asplund, M., Grevesse, N., Sauval, A. J., & Scott, P. 2009, ARA&A, 47, 481
Astropy Collaboration, Price-Whelan, A. M., Lim, P. L., et al. 2022, ApJ, 935, 167
Astropy Collaboration, Price-Whelan, A. M., Sipőcz, B. M., et al. 2018, AJ, 156, 123
Astropy Collaboration, Robitaille, T. P., Tollerud, E. J., et al. 2013, A&A, 558, A33
Barger, K. A., Lehner, N., & Howk, J. C. 2016, ApJ, 817, 91
Berg, D. A., James, B. L., King, T., et al. 2022, ApJS, 261, 31
Besla, G., Kallivayalil, N., Hernquist, L., et al. 2007, ApJ, 668, 949
Brüns, C., Kerp, J., Staveley-Smith, L., et al. 2005, A&A, 432, 45
Calzetti, D. 1997, in AIP Conf. Ser. 408, The Ultraviolet Universe at Low and High Redshift, ed. W. H. Waller (Melville, NY: AIP), 403
Chen, H.-W., Qu, Z., Rauch, M., et al. 2023, ApJL, 955, L25
Chen, Y.-M., Tremonti, C. A., Heckman, T. M., et al. 2010, AJ, 140, 445
Chisholm, J., Tremonti, C. A., Leitherer, C., & Chen, Y. 2017, MNRAS, 469, 4831
Chisholm, J., Tremonti, C. A., Leitherer, C., Chen, Y., & Wofford, A. 2016, MNRAS, 457, 3133
Chisholm, J., Tremonti, C. A., Leitherer, C., et al. 2015, ApJ, 811, 149
Choi, Y., Olsen, K. A. G., Besla, G., et al. 2022, ApJ, 927, 153

Choi, Y., Nidever, D. L., Olsen, K., et al. 2018, ApJ, 866, 90
Ciampa, D. A., Barger, K. A., Lehner, N., et al. 2021, ApJ, 908, 62
Danforth, C. W., Howk, J. C., Fullerton, A. W., Blair, W. P., & Sembach, K. R. 2002, ApJS, 139, 81
Davis, J. D., Tremonti, C. A., Swiggum, C. N., et al. 2023, ApJ, 951, 105
de Boer, K. S., Morras, R., & Bajaja, E. 1990, A&A, 233, 523
Erb, D. K., Quider, A. M., Henry, A. L., & Martin, C. L. 2012, ApJ, 759, 26
Freedman, W. L., Madore, B. F., Gibson, B. K., et al. 2001, ApJ, 553, 47
Gaustad, J. E., McCullough, P. R., Rosing, W., & Van Buren, D. 2001, PASP, 113, 1326
Gnat, O., & Sternberg, A. 2007, ApJS, 168, 213
Gordon, K. D., Clayton, G. C., Misselt, K. A., Landolt, A. U., & Wolff, M. J. 2003, ApJ, 594, 279
Hainich, R., Ramachandran, V., Shenar, T., et al. 2019, A&A, 621, A85
Harris, C. R., Millman, K. J., van der Walt, S. J., et al. 2020, Natur, 585, 357
Harris, J., & Zaritsky, D. 2009, AJ, 138, 1243
Hawcroft, C., Sana, H., Mahy, L., et al. 2024, A&A, 688, A105
Haydon, D. T., Kruijssen, J. M. D., Chevance, M., et al. 2020, MNRAS, 498, 235
Heckman, T. M., Alexandroff, R. M., Borthakur, S., Overzier, R., & Leitherer, C. 2015, ApJ, 809, 147
Heckman, T. M., Lehnert, M. D., Strickland, D. K., & Armus, L. 2000, ApJS, 129, 493
Hopkins, P. F., Kereš, D., Oñorbe, J., et al. 2014, MNRAS, 445, 581
Howk, J. C., Sembach, K. R., Savage, B. D., et al. 2002, ApJ, 569, 214
Hunter, J. D. 2007, CSE, 9, 90
Jenkins, E. B. 1996, ApJ, 471, 292
Kallivayalil, N., van der Marel, R. P., Besla, G., Anderson, J., & Alcock, C. 2013, ApJ, 764, 161
Kelly, B. C. 2007, ApJ, 665, 1489
Kennicutt, R. C., & Evans, N. J. 2012, ARA&A, 50, 531
Kim, C.-G., & Ostriker, E. C. 2017, ApJ, 846, 133
Kim, C.-G., & Ostriker, E. C. 2018, ApJ, 853, 173
Kim, C.-G., Ostriker, E. C., Somerville, R. S., et al. 2020, ApJ, 900, 61
Kim, S., Staveley-Smith, L., Dopita, M. A., et al. 1998, ApJ, 503, 674
Kim, S., Staveley-Smith, L., Dopita, M. A., et al. 2003, ApJS, 148, 473
Kroupa, P., & Weidner, C. 2003, ApJ, 598, 1076
Kudritzki, R.-P., & Puls, J. 2000, ARA&A, 38, 613
Lah, P., Colless, M., D'Eugenio, F., Groves, B., & Gelfand, J. D. 2024, MNRAS, 529, 2611
Lehner, N., & Howk, J. C. 2007, MNRAS, 377, 687
Lehner, N., Staveley-Smith, L., & Howk, J. C. 2009, ApJ, 702, 940
Li, M., Bryan, G. L., & Ostriker, J. P. 2017, ApJ, 841, 101
Martin, C. L. 2005, ApJ, 621, 227
Mazzi, A., Girardi, L., Zaggia, S., et al. 2021, MNRAS, 508, 245
McKee, C. F., & Ostriker, J. P. 1977, ApJ, 218, 148
McLeod, A. F., Dale, J. E., Evans, C. J., et al. 2019, MNRAS, 486, 5263
Medallon, S., & Welty, D. 2023, STIS Instrument Handbook for Cycle 31 v. 22
Morton, D. C. 2003, ApJS, 149, 205
Nidever, D. L., Majewski, S. R., & Butler Burton, W. 2008, ApJ, 679, 432
Oh, S.-H., Kim, S., Frr, B.-Q., & Staveley-Smith, L. 2022, ApJ, 928, 177

Olsen, K. A. G., & Massey, P. 2007, ApJL, 656, L61
Olsen, K. A. G., Zaritsky, D., Blum, R. D., Boyer, M. L., & Gordon, K. D. 2011, ApJ, 737, 29
Peeples, M. S., Corlies, L., Tumlinson, J., et al. 2019, ApJ, 873, 129
Poggianti, B. M., Fasano, G., Omizzolo, A., et al. 2016, AJ, 151, 78
Putman, M. E., Peek, J. E. G., & Joung, M. R. 2012, ARA&A, 50, 491
Putman, M. E., Zheng, Y., Price-Whelan, A. M., et al. 2021, ApJ, 913, 53
Rasmussen, C. E., & Williams, C. K. I. 2006, Gaussian Processes for Machine Learning (Cambridge, MA: MIT Press)
Rathjen, T.-E., Naab, T., Girichidis, P., et al. 2021, MNRAS, 504, 1039
Reichardt Chu, B., Fisher, D. B., Chisholm, J., et al. 2024, arXiv:2402.17830
Reichardt Chu, B., Fisher, D. B., Nielsen, N. M., et al. 2022, MNRAS, 511, 5782
Richter, P., de Boer, K. S., Werner, K., & Rauch, T. 2015, A&A, 584, L6
Richter, P., de Boer, K. S., Widmann, H., et al. 1999, Natur, 402, 386
Ripepi, V., Chemin, L., Molinaro, R., et al. 2022, MNRAS, 512, 563
Roman-Duval, J., Jenkins, E. B., Williams, B., et al. 2019, ApJ, 871, 151
Roman-Duval, J., Proffitt, C. R., Taylor, J. M., et al. 2020, RNAAS, 4, 205
Rubin, K. H. R., Prochaska, J. X., Koo, D. C., et al. 2014, ApJ, 794, 156
Rupke, D. S., Veilleux, S., & Sanders, D. B. 2005, ApJS, 160, 115
Rupke, D. S. N. 2018, Galax, 6, 138
Russell, S. C., & Dopita, M. A. 1992, ApJ, 384, 508
Salem, M., Besla, G., Bryan, G., et al. 2015, ApJ, 815, 77
Savage, B. D., & de Boer, K. S. 1981, ApJ, 243, 460
Savage, B. D., & Sembach, K. R. 1991, ApJ, 379, 245
Savage, B. D., & Sembach, K. R. 1996, ARA&A, 34, 279
Schaye, J., Crain, R. A., Bower, R. G., et al. 2015, MNRAS, 446, 521
Sembach, K. R., Wakker, B. P., Savage, B. D., et al. 2003, ApJS, 146, 165
Setton, D. J., Besla, G., Patel, E., et al. 2023, ApJL, 959, L11
Shull, J. M., Stevans, M., Danforth, C., et al. 2011, ApJ, 739, 105
Sirressi, M., Adamo, A., Hayes, M., et al. 2024, AJ, 167, 166
Skowron, D. M., Skowron, J., Udalski, A., et al. 2021, ApJS, 252, 23
Smart, B. M., Haffner, L. M., Barger, K. A., et al. 2023, ApJ, 948, 118
Soderblom, D. R. 2023, COS Instrument Handbook v. 15.0 (Baltimore, MD: STScI), 1515
Staveley-Smith, L., Kim, S., Calabretta, M. R., Haynes, R. F., & Kesteven, M. J. 2003, MNRAS, 339, 87
Tan, B., & Fielding, D. B. 2024, MNRAS, 527, 9683
Tchernyshyov, K. 2022, ApJ, 931, 78
van der Marel, R. P., Alves, D. R., Hardy, E., & Suntzeff, N. B. 2002, AJ, 124, 2639
Veilleux, S., Maiolino, R., Bolatto, A. D., & Aalto, S. 2020, A&ARv, 28, 2
Vogelsberger, M., Genel, S., Springel, V., et al. 2014, Natur, 509, 177
Wakker, B., Howk, J. C., Chu, Y.-H., Bomans, D., & Points, S. D. 1998, ApJL, 499, L87
Wakker, B. P. 2001, ApJS, 136, 463
Weiner, B. J., Coil, A. L., Prochaska, J. X., et al. 2009, ApJ, 692, 187
Werner, K., & Rauch, T. 2015, A&A, 584, A19
Xu, X., Heckman, T., Henry, A., et al. 2022, ApJ, 933, 222
Zheng, Y., Peek, J. E. G., Werk, J. K., & Putman, M. E. 2017, ApJ, 834, 179
Zhu, J., Tonnesen, S., & Bryan, G. L. 2024, ApJ, 960, 54